University of Alberta

On the Maximum Spreading Diameter of Impacting Droplets on Well-Prepared Solid Surfaces

by

Chijioke Ukiwe

A thesis submitted to the Faculty of Graduate Studies and Research in partial fulfillment of the requirements for the degree of **Master of Science.**

Department of Mechanical Engineering

Edmonton, Alberta

Fall 2004

Library and Archives Canada

Published Heritage Branch

395 Wellington Street
Ottawa ON K1A 0N4
Canada

Bibliothèque et Archives Canada

Direction du Patrimoine de l'édition

395, rue Wellington
Ottawa ON K1A 0N4
Canada

Your file Votre référence
ISBN: 0-612-95870-1
Our file Notre référence
ISBN: 0-612-95870-1

The author has granted a non-exclusive license allowing the Library and Archives Canada to reproduce, loan, distribute or sell copies of this thesis in microform, paper or electronic formats.

L'auteur a accordé une licence non exclusive permettant à la Bibliothèque et Archives Canada de reproduire, prêter, distribuer ou vendre des copies de cette thèse sous la forme de microfiche/film, de reproduction sur papier ou sur format électronique.

The author retains ownership of the copyright in this thesis. Neither the thesis nor substantial extracts from it may be printed or otherwise reproduced without the author's permission.

L'auteur conserve la propriété du droit d'auteur qui protège cette thèse. Ni la thèse ni des extraits substantiels de celle-ci ne doivent être imprimés ou aturement reproduits sans son autorisation.

In compliance with the Canadian Privacy Act some supporting forms may have been removed from this thesis.

While these forms may be included in the document page count, their removal does not represent any loss of content from the thesis.

Conformément à la loi canadienne sur la protection de la vie privée, quelques formulaires secondaires ont été enlevés de cette thèse.

Bien que ces formulaires aient inclus dans la pagination, il n'y aura aucun contenu manquant.

Canada

"When Jesus therefore had received the vinegar, he said,

It is finished: and he bowed his head,

and gave up the ghost"

– John 19:30

To:

Vincent Onyemaechi Ukiwe

(April 19, 1974 – January 23, 2004)

&

The Almighty God – the Ancient of Days,

who knoweth all things.

ACKNOWLEDGEMENTS

Many people helped and encouraged me to bring this thesis to completion, and I am so grateful to all of them. If I have inadvertently omitted anyone, I apologize for the absentmindedness.

I would like to thank, first and foremost, my indefatigable supervisor, Dr. Daniel Y. Kwok, for his patience, understanding, and thorough guidance that saw this thesis to completion. Worthy of mention is his unparalleled willingness to offer helpful suggestions even at odd hours! I will also not fail to recognize the helpful suggestions from my group members at the Nanoscale Technology and Engineering Lab., especially Kelvin Isaacson, who offered some assistance when the LINUX operating system would have driven me crazy at the beginning.

To my parents, Mr. Ukiwe & Mrs. Grace Anya Kalu, I am highly appreciative for prayers, support, and godly guidance that saw me through those many years of education in Nigeria which earned me a first degree in mechanical engineering at the at the University of Nigeria, Nsukka. They should be proud – but perhaps confused and surprised – to read this thesis on tiny, liquid droplets and solid surfaces!

I am equally grateful to my brothers and sisters and their spouses (Chukwuma & Jane, Nnenna & Ifendu Ukonu, Jane & Ndukwe Ogbugo, Ivan & Nnenna Anya, and Nwanne & Kalu Amogu) who are currently in Nigeria, for their prayers and varied support.

I am no less thankful to my good friend and "big brother-in-Edmonton", Ken Nnamoko and his wife *Akwa Nwa* Oby, for sacrifices and support; and my uncle Mr. Henry A. Ajike (Dallas, Texas) for his timely financial

aids before I came to Edmonton, and even during my studies. Thank you very much.

And to my very best friend and Sweetheart, *Onye nkem* Ijeoma Ikodiya, I am forever grateful for her pleasant understanding, prayers and patience.

How else could I possibly close these avalanche of *thank-yous* except to give all the glory, honor, adoration and thanksgiving to the Almighty God for His mercies and to pray that His blessings be bestowed on everyone – acknowledged here or not – who has been helpful in seeing this work to completion?

CONTENTS

1 INTRODUCTION AND LITERATURE REVIEW **1**

1.1 Overview 1

1.2 Parameters affecting the behavior of impacting droplets 2

1.3 Previous Work 7

1.4 Motivation 9

1.5 Outline of the thesis 10

2 TAILORED SURFACE ENERGETICS AND THE DYNAMICS OF DROP IMPACT **12**

2.1 Introduction 12

2.2 Method and Materials 14

2.2.1 Self-Assembled Monolayers 14

2.2.2 Materials 15

2.2.3 Preparation of SAMs 15

2.2.4 Cleaning Procedure 16

2.2.5 Droplet imaging system 17

2.2.6 Characterization of SAMs 20

2.2.7 Parameters for Impact 21

2.3 Results and Discussion 22

2.3.1 Surface Characterization by FT-IR, AFM, Ellipsometer and Contact angle . . . 22
2.3.2 Observation of spreading phenomenon . . . 25
2.3.3 Surface wettability and model predictions . . . 29
2.4 Conclusions . . . 37

3 PREDICTING THE MAXIMUM SPREADING DIAMETER 40
3.1 Introduction . . . 40
3.2 Method and Materials . . . 42
3.3 Results and Discussion . . . 44
3.3.1 Droplet Collision Dynamics . . . 44
3.3.2 Model Predictions and Experimental Data . . . 49
3.4 Conclusions . . . 61

4 ON WETTABILITY AND THE MAXIMUM SPREADING DIAMETER 63
4.1 Introduction . . . 63
4.2 Experimental Procedures . . . 64
4.3 Results and Discussion . . . 66
4.3.1 Surface Characterization using FT-IR and ADSA-P . . . 66
4.3.2 Droplet Impact Scenario . . . 68
4.3.3 Estimating the Maximum Spreading Diameter . . . 74
4.4 Conclusions . . . 77

5 Conclusions and Recommendations 79
5.1 Conclusions . . . 79

5.2 Recommendations 80

Bibliography **86**

List of Tables

2.1 Impact velocities and other dimensionless parameters for water droplets ($D_0 = 3.6280$ mm). 21

2.2 Sequential images of the impacting water droplets onto the Au/S(CH_2)-$_{15}CO_2H$ (CO_2H) and Au/S$(CH_2)_{17}CH_3$ (CH_3) surfaces at different temporal resolutions for two Weber numbers, 37 and 60. 39

3.1 Summary of the advancing contact angle θ_a and solid-vapor surface tension γ_{sv} from [1] for poly(methyl methacrylate) PMMA, poly(methyl methacrylate/n-butyl methacrylate) P(nBMA/MMA) and poly(n-butyl methacrylate) PnBMA 44

3.2 Impact velocities and other dimensionless parameters for water and formamide droplets. D_0 is the initial droplet diameter. 46

3.3 Summary of error analysis of the model predictions for our experimental data. 61

4.1 Advancing contact angle of water θ_a (degree) and solid-liquid work of adhesion W_{sl} (mJ/m^2) for mixed SAMs. The dimensionless time $\tau = tU/D_0$ to reach a maximum spreading ratio and an initial spreading film velocity u_e/U during the first 4.4 ms are also shown. 67

4.2 Summary of error analysis for the prediction of maximum spreading factor β_{max} from different models. 76

5.1 Impact velocities and other dimensionless parameters for water ($D_0 =$ 3.6280 mm). U_n is determined from Eq. (5.7) while We_n is calculated using U_n 84

List of Figures

1.1 Schematic of a sessile drop contact angle system 4

2.1 Schematic representation of a typical self-assembled monolayer adsorbed onto a metal or metal-oxide support. 16

2.2 Schematic representation of a typical self-assembled monolayer adsorbed onto a metal or metal-oxide support. 17

2.3 Schematic of the experimental set-up 18

2.4 FT-IR spectra of $Au/S(CH_2)_{17}CH_3$ 22

2.5 FT-IR spectra of $Au/S(CH_2)_{15}CO_2H$ 23

2.6 3-D AFM image of $Au/S(CH_2)_{17}CH_3$ surface 24

2.7 3-D AFM image of $Au/S(CH_2)_{15}CO_2H$ surface 25

2.8 Ratio of the maximum spreading diameter of CH_3 $D_{max(CH_3)}$ to that of CO_2H $D_{max(CO_2H)}$ versus the impact Weber number. The effect of inertia is shown to dominate surface tension effect as the impact Weber number increases. 27

2.9 Time evolution of spreading factor $\beta(t)$ of water impacting onto the CH_3 and CO_2H surfaces. 33

2.10 Time evolution of spread factors of water on impact at $We = 466$ on CH_3 and CO_2H surfaces. Results for the Roisman et al [2] model could not be computed for the CO_2H surface because the term $\bar{\tau}$ in Eq.(2.15) results in a complex square root. 35

3.1 Sequential images of a 2.7107 mm water droplet impacting on PMMA, P(nBMA/MMA) and PnBMA surfaces at an impact velocity U = 0.7059 m/s. Contact angles θ_Y and solid-vapor surface tensions γ_{sv} were obtained from [1]. 45

3.2 Sequential images of a 2.7107 mm water droplet impacting on PMMA, P(nBMA/MMA) and PnBMA surfaces at an impact velocity U = 1.4119 m/s. The differences in the behavior of water droplets were due to incremental variations of the solid-vapor surface tensions γ_{sv}. Contact angles θ_Y and solid-vapor surface tensions were obtained from [1]. 47

3.3 Sequential images of a 2.5296 mm formamide droplet on PMMA, P(nBMA-/MMA) and PnBMA surfaces at an impact velocity $U = 2.1178$ m/s. The differences in the behavior of formamide droplets were due to incremental variations of the solid-vapor surface tensions γ_{sv}. Contact angles θ_Y and solid-vapor surface tensions were obtained from [1]. . . 48

3.4 Comparison of the model prediction by Madejski [3] and the modified Madejski model by Benneth and Poulikakos [4] with our experimental results. The relative mean error for the Madejski model (circles) is 54.54 $\pm$ 5.53% and that for the modified Madejski model (filled squares) is 62.66 $\pm$ 5.74%. 50

3.5 Comparison of the model by Roisman et al. [2] with our experimental results. The relative mean error is 12.29 ± 6.69%. 52
3.6 Comparison of the modified K-Y model [5] with our experimental results. The relative mean error is 7.10 ± 5.79% 53
3.7 Model proposed in Ref. [6] for the spreading droplet. This figure has been exaggerated for clarity: $D(t) \gg h$ 54
3.8 Comparison of the Pasandideh-Fard et al. model [6] with our experimental results. The relative mean error is 6.57 ± 7.33%. 56
3.9 An idealized cylindrical model for the maximum spread diameter. . . 57
3.10 Comparison of Eq.(3.10) [our modified model] with (a) our experimental data and (b) results from data used in Ref. [6]. The relative mean error for (a) is 4.97 ± 5.05%. 60

4.1 Grazing incident polarized infrared spectra for mixed SAMs of 16-mercaptohexadecanoic acid and 1-octadecanethiol in four different ratios. The approximate positions of methylene modes are 2918(asym) cm^{-1} and 2850(sym) cm^{-1}, and those for the methyl modes are 2964(asym) cm^{-1}, and 2879(sym) cm^{-1}. The spectra have been offset vertically for clarity. 66
4.2 Impact of water droplets on mixed SAMs of 1-octadecanethiol and 16-mercaptohexadecanoic acid in CH_3:CO_2H volume fractions of 10:90, 30:70, 50:50 and 70:30. θ_a is the advancing contact angle of water (continued on next page) 70
4.2 Impact of water droplets on mixed SAMs of 1-octadecanethiol and 16-mercaptohexadecanoic acid in CH_3:CO_2H volume fractions of 10:90, 30:70, 50:50 and 70:30. θ_a is the advancing contact angle of water. . . 71

4.3 Axial rebound for mixed SAMs of 1-octadecanethiol and 16-mercaptohexade-canoic acid at $t = 32$ ms after impact. The fractions represent relative volume percentages of CH_3:CO_2H and W_{sl} is the thermodynamic solid-liquid work of adhesion in mJ/m^2. 72

4.4 Time evolution of droplet spreading diameter $\beta(t)$ on mixed SAMs with CH_3:CO_2H volume fractions of 10:90, 30:70, 50:50, and 70:30. . . 73

4.5 Maximum spreading factor β_{max} for mixed SAMs as a function of the percentage of 16-mercaptohexadecanoic acid monolayers CO_2H. . . . 74

4.6 Hypothetical situation depicting the influence of wettability, defined by the Young contact angle θ_Y, on the maximum spreading diameter β_{max}. Eq.(3.10) was used to generate the curves for (a) $We = 60$, (b) $We = 150$, (c) $We = 500$ and (d) $We = 1000$, for different Reynolds numbers, $1000 \leq Re \leq 15{,}000$. 77

4.7 Hypothetical situation depicting the influence of wettability, defined by the Young contact angle θ_Y, on the maximum spreading diameter β_{max} for $Re = 1000$ and $We = 60$, 150, 500 and 1000 according to Eq.(3.10). 78

5.1 Effect of drag and buoyancy on the falling droplet 83

NOMENCLATURE

a_0 ..... thermal diffusivity

a ..... acceleration of interface between two fluids of diferent densities

b ..... "drag coefficient" ($\equiv 6\pi\mu D_0/2$)

Ca ..... Capillary number

d ..... diameter of liquid flow in modeling droplet spread

D_{max} ..... Maximum spreading diameter

D_0 ..... Droplet diameter before impact

$D(t)$ ..... Time-dependent diameter

E_{k_i} ..... Kinetic energy before impact

E_{s_f} ..... Surface energy at maximum spread

E_{s_i} ..... Surface energy at before impact

F_g, F_b, F_d .. Gravitational, buoyant and drag force on a falling droplet

g ..... acceleration of gravity

h ..... height of the liquid film above the solid surface

m ..... Mass of droplet

N ..... Number of fingers formed around a spreading droplet

P ..... Pressure

Re ..... Reynold number ($\equiv \rho U D_0/\mu$)

t ..... Time

T ..... Temperature

t_c ..... Dimensionless time to reach maximum spread

U ..... Velocity of impact

u_e ..... Spreading velocity

W ..... Energy lost to viscous energy dissipation

We ..... Weber number ($\equiv \rho U^2 D_0/\gamma_{lv}$)

W_{sl} ..... Solid-liquid work of adhesion

$\beta(t)$, β_{max} .. Time-varying and maximum spreading ratio($\equiv D(t)/D_0$, D_{max}/D_0)

δ ..... Boundary layer thickness

γ_{sv},γ_{lv},γ_{sl} ... Solid-vapor, liquid-vapor, and solid-liquid interfacial tentions

λ ..... wavelength of interfacial waves in a spreading droplet

μ ..... Dynamic viscosity

$\theta, \theta_Y, \theta_a$ .... Contact angle, Young's contact angle and dynamic advancing contact angle

Ω ..... Volume

ρ ..... Density

τ ..... Dimensionless Time ($\equiv tU/D_0$)

CHAPTER 1

INTRODUCTION AND LITERATURE REVIEW

1.1 Overview

The impact of liquid droplets on solid surfaces plays an important role in many practical processes. It is therefore of technological concern in several contexts, namely, ink-jet printing, spray cooling of hot surfaces [1, 2, 3], spray forming and spray coating [4, 5, 6], fuel injection in internal combustion engines, insecticides and pesticides, fire-suppression by sprinkler systems, and a host of others. To enhance efficiency in these applications, a detailed understanding of the fluid dynamics of the liquid droplets during and after impact on the surfaces is therefore required. For the spray cooling of hot surfaces, for example, it is required that the spread of the liquid film on the surface be a maximum so that the area of the liquid exposed to the surface for transfer of heat be a maximum. In addition, it is also desired that the duration of the droplets on the surface be a minimum, ensuring that new droplets impinge on the same spot, so making room for enhanced heat flux. On the other hand, for spray of insecticides on foliage, it is desired that the droplets spread on the surface be maximum and that they remain on the surface.

Of vital importance, therefore, in the study of impacting droplets on solid surfaces is the ability to tailor the surfaces for specific physical properties, characterize

them for various chemical and physical functionalities and record the dynamics of the liquid droplets during the deformation stages. These areas of study will be carefully considered in this thesis.

The practical applications mentioned above employ multiple streams of droplets. However, a detailed analysis of the collision dynamics requires that attention be focused on a single droplet-surface interaction. Like many other studies, this is the approach adopted in this thesis. Typically, when a liquid droplet impinges on a rigid surface it undergoes rapid deformation. This deformation could result in several outcomes, including spreading, recoiling, splashing, and/or solidification. However, the outcome of the drop impact depends on a host of system parameters related to the liquid droplet and the solid surface. These parameters are explored in the section that follows.

1.2 Parameters affecting the behavior of impacting droplets

Drop impact processes typically involve three phases, namely, the solid surface, the liquid droplet, and the surrounding gas in the near-solid region. It is therefore expected that collision dynamics will be influenced by the physical properties of the liquid droplet, the physical properties and wettability of the solid surface, and the characteristics of the gas near the solid surface. These physical properties are given below.

- *Solid surface properties*
  - *Surface roughness.* Several workers have examined the effect of surface roughness on the behavior of impacting droplets [7, 8]. In most cases they examined splashing threshold and the formation of secondary droplets upon drop impingement. It has been shown that the number of satellite

droplets formed depends largely on surface roughness parameter.

- *Inertness.* Drop impact studies could be somewhat difficult if the solid surface reacts with the impinging droplets. The implication is that an additional degree of freedom is introduced in the drop impact process, and it becomes more difficult to isolate the effect of chemical reaction due to drop impact.

- *Surface temperature.* The temperature of the target substrate is very important during the drop impact process. As mentioned earlier, one of the areas of application of impinging droplets is the spray cooling of hot surfaces. A lot has already been done on the dynamics of droplets impinging on heated surfaces [9, 10, 11, 12, 13, 14, 15].

- *Surface Wettability.* This remains one of the most important properties in the drop impact problem. It is commonly represented by the angle of contact between the solid surface and the liquid droplets. More specifically, the contact angle of a liquid droplet on a solid surface is defined by the mechanical equilibrium of the drop under the action of three interfacial tensions (see Figure 1.1): solid-vapor, γ_{sv}, solid-liquid, γ_{sl}, and liquid-vapor, γ_{lv}. This equilibrium condition is known as Young's equation:

$$\gamma_{lv} \cos\theta_Y = \gamma_{sv} - \gamma_{sl}, \tag{1.1}$$

where θ_Y is the Young contact angle, i.e. an equilibrium contact angle that can be used in conjunction with Eq. (1.1). For one and the same liquid droplet impacting on different surfaces (defined by varying Young contact angles) at the same impact velocity, the spreading behavior of the droplet is bound to be different for every surface. In particular, the droplet is

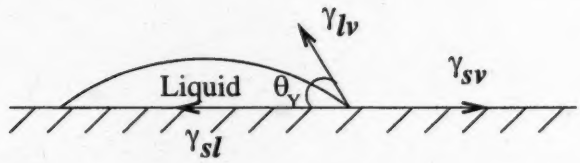

Figure 1.1: Schematic of a sessile drop contact angle system .

expected to spread more readily on the surfaces with lower contact angles due to stronger solid-liquid affinity.

- *Solid surface tension* γ_{sv}. This property has been defined above with respect to the Young's Eq. (1.1). It is one of the most difficult properties to characterize. In fact, most of the studies in the literature for drop impact have not characterized their target surfaces for γ_{sv} because no direct methods are available to determine the interfacial tension of most practical surfaces. Changing γ_{sv} for the impact of one amd the same liquid can significantly change the drop impact dynamics, as will be shown in this work.

- Liquid droplet properties

  - *Density*. This property has direct relevance to the impact energy of the droplet and the capillary forces that account for the spreading and recoil process.

  - *Viscosity*. This parameter displays its effect in accounting for additional energy loss during droplet spread. A higher viscosity liquid tends to resist liquid spread inertia via viscous energy dissipation. Thus, higher energy impact is required to achieve a desired droplet spread, if all other parameters are kept constant.

  - *Chemical structure*. A previous study on contact angle measurement of

several liquids on some solid surfaces [poly(methyl methacrylate), poly(*n*-butyl methacrylate), poly(*n*-butyl methacrylate /methyl methacrylate)] has shown that some of the liquids used in their study dissolved the solids on contact [16]. This points to the importance of the chemical structure of the liquids with respect to the solid surfaces, and requires that the solid surface be inert with respect to the impacting liquid droplets.

- *Liquid surface tension,* γ_{lv}. This is a thermodynamic property of the liquid, characterizing the resistance to the formation of additional surface area. Thus, it plays a predominant role during the spreading and recoil process after drop impact. As given by Eq. (1.1), it is also important for the determination of the solid-liquid contact angle, and hence, the wetting characteristics of the system.
- *Droplet size,* D_0. The effect of droplet size is important in several contexts. The impact kinetic energy increases with droplet size. This has direct implication on the impact pressure exerted on the solid surface. Moreover, the effect of surface tension is more critical for smaller droplet sizes. It is therefore expected that droplet spread may be impeded more when the droplet size is smaller. In addition, droplet recoil is also expected to be higher due to increased influence of surface tension on the smaller droplets.
- *Droplet velocity,* U. It was mentioned earlier that the impact process could result in several outcomes. These outcomes are also directly related to the impact velocity. The impact energy, as we know it, increases with impact velocity.

- *Surrounding gases*

The properties of the surrounding gases can affect the behavior of the impacting

droplets in a number of ways. For example, if the gases possess a non-zero velocity, the direction of the velocity can affect the impact dynamics. Other factors of the surrounding gas that can affect the drop impact process are the density, humidity and temperature.

The foregoing parameters give rise to a host of dimensionless numbers which are representative of most droplet impact studies. These nondimensional parameters include:

- The spreading ratio, $\beta(t)$, defined as the ratio of the time-varying droplet diameter to the original diameter [$\beta = \frac{D(t)}{D_0}$]. It is an important parameter for general comparison with other literature data, especially when different drop diameters are used in conjunction with other process parameters.

- The Weber number, We, given as:

$$We = \frac{\rho U^2 D_0}{\gamma_{lv}}, \tag{1.2}$$

  The Weber number depicts the ratio of inertia to surface tension forces. It measures the relative importance of surface tension to the droplet inertia.

- The Reynolds number, Re, which represents the ratio of inertia to viscous forces. It also reflects the effects of hydrodynamics on the spreading process. It is defined as

$$Re = \frac{\rho U D_0}{\mu}, \tag{1.3}$$

  where μ is the liquid dynamic viscosity.

- The capillary number, Ca, defined by the relation:

$$Ca = \frac{We}{Re} = \frac{\mu U}{\gamma_{lv}}. \tag{1.4}$$

It defines the relevance of surface tension in droplet recoil motion after reaching the maximum spreading diameter.

1.3 Previous Work

One of the earliest studies on the behavior of impacting droplets was performed by Worthington [17] over a century ago. In that pioneering work he examined the fingering patterns of milk and mercury drops as they impacted on smoked glass. Following his study, several other authors have researched the behavior of impacting droplets, including numerical modeling [13, 18, 19, 20] and analytical technique [21, 22] for droplet impact, experimental studies of solidification of droplets upon impact [13, 20, 23, 24], effect of surfactants [25, 26, 27] and wetting [20, 28, 29, 30, 31, 32] on droplet impact, and cooling of hot surfaces [10, 11, 12, 14, 25, 33, 34, 35, 36, 37, 38]. A review of droplet impact problem on solid and liquid surfaces is available elsewhere [39].

In most practical situations, the properties of the impacting liquid pose no special difficulty. The solid surface, however, is the center-point of experimental errors. As mentioned above, the dynamics of droplets impinging on solid surfaces have been examined extensively using several approaches, including, for example, numerical methods. Validation of the accuracy of the numerical results are often made by comparison with experimental data either from literature or from the authors' own experiments. It is therefore required that, to make a reasonable assessment of these numerical schemes, the data obtained from the experiments are reliable. Besides

numerical methods, other authors have developed models to account for either the time evolution of the spreading diameter or the maximum spreading diameter [11, 17, 29, 40, 41, 42, 43, 44, 45]. Again, these models had to be tested for validity using experimental data. Reliability of these experimental data, it must be emphasized, is closely tied to several factors, namely: reliable solid surface preparation, accurate acquisition of data on the spreading droplets, and ability to characterize the solid surfaces with which the droplets collide. However, our observations show that most studies have not given special consideration to the quality of the solid surfaces used in drop impact experiments. In this sense, the fact is that no study presented results for well-characterized solid surfaces prior to drop impact. This implies that consistency and accuracy is, in a way, sacrificed.

On a closer look, the models mentioned above for predicting the spreading diameters are based on several assumptions. In most cases, energy conservation principle is used for the droplets during spread. However, it is difficult to agree on a more generally acceptable model based on these assumptions if the experimental data are not reliable. For example, some workers assume that wettability may be neglected during drop impact [23, 43, 46]. Some of these workers may have reached such conclusions after comparing their models with experimental data obtained from non-characterized solid surfaces. However, as adsorption of contaminants (hydrocarbons) on high energy surfaces occurs readily under ambient conditions, interpretation of impact dynamics data and comparing them with model studies (in an attempt to verify model assumptions and predictive capability) can be misleading and complicated. For example, while Fukai et al. [20] showed from numerical and experimental study that wettability affects droplet spreading throughout the spreading phase, Richard [47] and Mao et al [48] observed no variation in the maximum spreading diameter for different surfaces (supposedly with varying contact angles). The only possible explanation for

the anomaly in the second group of studies must be that their solid surfaces might have been chemically changed due to, e.g., physico-chemical adsorption or roughness of such surfaces dominated. Hence, there was no observable difference in the drop impact dynamics.

Besides the assumptions of negligible wettability, the other notable contention in literature models is the lack of appropriate model for the viscous energy dissipation and the surface energy at the maximum spread. But the fact remains that the "universality" of any model prediction can only be ascertained with respect to reliable data obtained from well-characterized solid surfaces. In the course of this thesis, more extensive literature review is presented to drive home the points introduced here.

1.4 Motivation

This thesis is motivated firstly by the desire to present reliable experimental data on well-characterized solid surfaces for droplet impact. Secondly, we shall examine literature models that predict the behavior of impacting droplets with respect to the spreading ratio for both time-dependent droplet spread and for the maximum spreading diameter of such droplets. The intent is to ascertain the validity of literature assumptions on the collision dynamics of spreading droplets. Hence, a veritable conclusions can be reached on reasonably accurate underlying assumptions on the most reliable spreading models with a view to developing a more universal one.

As part of this work, therefore, we shall follow a very careful solid surface preparation procedure. In addition, we shall also characterize the target substrates using techniques such as Variable Angle Spectroscopic Ellisometry (VASE), Fourier Transform Infrared Spectroscopy (FT-IR), and Atomic Force Microscopy (AFM). These tools will be used to probe the surface composition, structure, and morphology before the impact process. The Axisymmetric Drop Shape Analysis Profile (ADSA-P)

technique will be used to characterize surface wettability by the determination of the advancing contact angle, and hence, the solid surface tension using an equation of state approach [16, 49, 50, 51]. Finally, high speed video imaging will be employed to record the dynamics of the impacting processes.

It is hoped that the experimental data presented in this work can be used to verify the accuracy of literature models for predicting droplet dynamics.

1.5 Outline of the thesis

The discussion that follows after this introductory chapter involves the use of several parameters, both dimensional and dimensionless ones. These have been given in the nomenclature to avoid ambiguities. Whenever appropriate, some parameters are redefined for clarity. This thesis has been organized in the following manner according to the chapters.

Chapter 2 is concerned with the dynamics of impacting water droplets on tailored surfaces using two self-assembled monolayers (SAMs): a hydrophilic 16-mercaptohexadecanoic acid and a hydrophobic 1-octadecanethiol. The two surfaces differ in their chemical functionality by the end-functional group, and these change the behavior of the droplets during impact on the surfaces. All relevant surface preparation methods and cleaning procedures are outlined in detail. In addition, the image capture system is described in detail together with the method of data acquisition and analysis. Since the solid surfaces are characterized before the impacting droplet experiments, the characterization tools and techniques are also described. The experimental results are compared with two literature models to verify the accuracy of these predictions in modeling the dynamics of water droplets on our well-characterized solid surfaces.

In Chapter 3, we adopt a more qualitative approach to examine the problem of drop impact dynamics on well-prepared and well-characterized solid surfaces us-

ing three polymer surfaces: poly(methyl methacrylate), poly(methyl methacrylate/*n*-butyl methacrylate) and poly(*n*-butyl methacrylate). These surfaces were prepared through careful experimental procedures that were used for the determination of solid surface tensions from contact angles. Our data for the maximum spreading diameter of water and formamide impacting on these surfaces were compared with those predicted from literature models. Of the models selected, we modified the model of Pasandideh-Fard et al. [*Phys. Fluids*, 8 (1996) 650] and the results for the maximum spreading diameter were in good agreement with our experimental data and that from literature.

The impact of water droplets (diameter: 3.6280 mm) at a fixed Weber number of 60 on solid surfaces with precisely tailored surface wettabilities is presented in Chapter 4. Solid surface wettability was varied using four fractional mixtures of self-assembled monolayers of 1-octadecanethiol and 16-mercaptohexadecanoic acid. The surfaces so obtained are characterized for contact angle and chemical functionality using axisymmetric drop shape analysis-profile (ADSA-P) technique and Fourier Transform Infra-red Spectroscopy (FT-IR). The results correlate the wetting effects of the impacting droplets with the surface energy and contact angle measurements of the tailored surfaces.

Finally, Chapter 5 gives conclusions and recommendations for future work.

CHAPTER 2

TAILORED SURFACE ENERGETICS AND THE DYNAMICS OF DROP IMPACT

2.1 Introduction

Several authors have acknowledged that a detailed analysis of impacting droplets is difficult [8, 39] as there can be many competing process parameters to be accounted for. Specifically, the properties of the fluid, solid and fluid-solid interface should all be considered. It is commonly assumed that these fluid properties include density ρ, viscosity μ, droplet diameter D_0, velocity U and liquid-vapor surface tension γ_{lv}; those of the solid surfaces are chemical heterogeneity and surface roughness. While we believe that solid-liquid adhesion strength or interfacial properties should also have a profound effect on droplet impact, most experimental studies performed have neglected these important factors, i.e., solid surface energetics. For instance, numerical simulations by Healy [52] indicated that droplet spreading process is highly dependent on the Weber number ($We \equiv \rho U^2 D_0/\gamma_{lv}$), Reynolds number ($Re \equiv \rho U/\mu$) and the contact angle θ. As contact angle relates the interfacial tensions between the solid-vapor γ_{sv}, liquid-vapor γ_{lv} and solid-liquid γ_{sl} interfaces, droplet dynamics in terms of γ_{sv} should be considered. However, surface roughness can complicate the

interpretation as it also affects the phenomenological contact angles. Further, it is not an easy task to isolate surface roughness and examine the independent effect of γ_{sv} on θ (and hence droplet impact) experimentally. This is due to the difficulty in characterizing real surfaces. Thus, the first objective of this paper is to illustrate the importance of surface characterizations for the underlying physics of droplet dynamics upon impact onto surfaces.

In the literature, there are a number of indirect references to the effect of solid surface tension on droplet dynamics. However, most numerical studies account for the fluid dynamics of different liquid droplets on various solid surfaces via a constant contact angle which is imposed as a boundary condition in their simulations. For example, Figure 1 in Ref. [24] illustrates that changing the equilibrium contact angles can have significant effects on the spread of an impacting droplet. More recently, et al [53] performed an extensive experimental study of the influence of wettability (contact angle) and surface roughness on spreading, by classifying droplet spread into several phases and analyzed the behavior of the droplet within each phase under different conditions. Our work presented here is similar to that in [53], except that we have characterized more rigorously the solid surfaces used in our experiments. It will be illustrated that surface energetics and hence droplet spread can be significantly different even when there is only a small variation in chemical functionality ($\sim$ 2 Å) of the surfaces. Our results presented here have important implication on literature data of droplet impact dynamics onto surfaces which have not been well-prepared and characterized.

In this chapter, we also examine the controlling factors for the dynamics of water droplet impact onto tailored surfaces with respect to the morphology and chemical structure. Several experimental and numerical studies have been performed to unravel the problem of drop impact with respect to solid surface wettability. However,

systematic account for the observed behavior in terms of solid surface properties is only available in terms of the three-phase contact angle (which defines wettability) and surface roughness. This chapter takes these investigations a step further by characterizing the solid surfaces, probing the chemical structure and morphology, providing the links between the physics of the drop impact dynamics, chemistry of the solid surface and their surface nanostructure. The surface tensions of the substrates are modified indirectly by means of surface chemistry via a so-called self-assembled monolayers (SAMs) [54, 55, 56, 57, 58], giving varying degrees of wettability. Chemically, the generated surfaces differ only by the terminal functional group on the order of 2 Å. The outcome of such a modification leads to different behavior in terms of drop impact dynamics. Fourier Transform Infrared Spectroscopy (FT-IR) and Variable Angle Spectroscopic Ellipsometry (VASE) will be used to determine chemical functionality and thickness of the SAMs, respectively. Atomic Force Microscopy and contact angle will be employed to characterize the surface roughness and wettability (surface hydrophobicity), respectively. As a second objective, our results for spreading dynamics will also be compared with both semi-empirical (Shi and Chen [46]) and analytical (Roisman et al [59]) models. It will be shown that none of these models is capable of predicting the variation of spreading ratio for water droplet on carefully prepared surfaces.

2.2 Method and Materials

2.2.1 Self-Assembled Monolayers

SAMs are two dimensional organic assemblies (Figure 2.1) that form by chemisorption and self-organization of functionalized long-chain organic molecules onto the surfaces of appropriate substrates [57]. They are typically prepared by directly immersing the

substrate into a solution containing a ligand that is reactive toward the surface, or by exposure to the vapor of the reactive species [57]. SAMs are particularly useful because their biological and organic properties are easily manipulated by tailoring the end functional group. Thus, they provide model systems for the study of a range of technological systems where interfacial phenomenon play a dominant role. Two types of SAMs have been selected in this study: a hydrophobic 1-octadecanethiol $HS(CH_2)_{17}CH_3$ and a hydrophilic 16-mercaptohexadecanoic acid $HS(CH_2)_{15}CO_2H$. The former is a monolayer with a methyl terminal group ($-CH_3$) and that of the latter with a carboxylic group ($-CO_2H$). In both cases, the functional group for attachment to metal surfaces is the sulphide group ($-SH$). Our choice of these SAMs was based on their wide range of wettability.

2.2.2 Materials

Octadecanethiol $HS(CH_2)_{17}CH_3$ (98%) and 16-mercaptohexadecanoic acid HS-$(CH_2)_{15}CO_2H$ (90%) were purchased from Aldrich and used as received. Deionized ultra-filtered water (DIUF) was obtained from Fisher Scientific was used to generate the liquid droplets for drop impact and for cleaning of apparatus.

Silicon (Si) wafers were obtained from Wafer World (West Palm Beach, FL), as test grade in circular discs of about 10 cm diameter. We purchased Gold (99.999%) and Titanium shots (99.95%) from Kurt J. Lesker (Clairton, PA) and ethanol (100%) from the Chemistry Dept. at the University of Alberta.

2.2.3 Preparation of SAMs

Several methods are available for preparing thin gold (Au) film. Of these methods, the most popular remains evaporation of Au onto Si wafer. However, the adhesion between the deposited Au film and the Si support is weak; thus necessitating the use

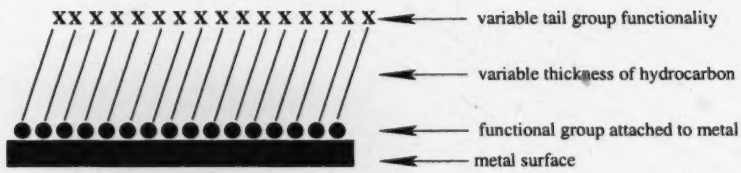

Figure 2.1: Schematic representation of a typical self-assembled monolayer adsorbed onto a metal or metal-oxide support.

of an interlayer. Often, titanium of $\sim$ 10 nm is often used to enhance adhesion. The gold films we used were prepared by sequentially evaporating titanium ($\approx$ 10 nm) and gold ($\approx$ 100 nm) onto the circular disc silicon wafers in a diffusion-pumped vacuum chamber at a rate of $\leqslant$ 2 Å/s under $\approx 2 \times 10^{-6}$ Torr. (see Figure 2.2). The chamber was backfilled with air and the substrates were used within 48 hr of preparation. The evaporated surfaces were then cut into smaller pieces of approximately 2.5 cm $\times$ 5 cm and rinsed with ethanol before SAMs formation. For the purpose of contact angle measurements, holes of about 1 mm diameter were made using a diamond drill bit from Lunzer (New York, N.Y.; SMS-0.027), in the center of each wafer surface and cleaned thoroughly using acetone before the process of evaporation. SAMs were prepared by immersing the test pieces into 5 mM ethanol solutions of either $HS(CH_2)_{17}CH_3$ or $HS(CH_2)_{15}CO_2H$ for at least 6 hr. The resulting surfaces were rinsed with ethanol and blow dried by nitrogen before use.

2.2.4 Cleaning Procedure

With respect to the drop impact experiments, the cleaning procedures are critical as surface tensions are known to be extremely sensitive to minute impurities and contaminants. The hypodermic needle, syringe, and other sensitive connectors were placed in a cleaned glass beaker and submerged with denatured alcohol solution containing 85% ethanol and 15% methanol (Fisher Scientific), covered with aluminum

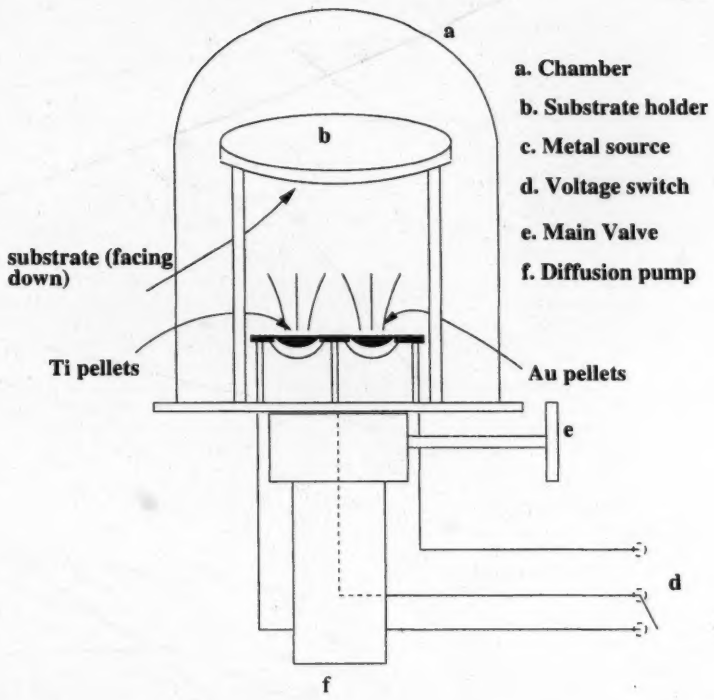

Figure 2.2: Schematic representation of a typical self-assembled monolayer adsorbed onto a metal or metal-oxide support.

foil, and placed in a sonicator (Aquasonic Model 75D, VWR Scientific Products) for 15 min. The liquid is poured out and the process repeated with fresh ethanol solution before finally rinsing with DIUF water and placed in the sonicator again for 10 min. The contents are then dried under a heat lamp before use.

2.2.5 Droplet imaging system

Figure 2.3 displays a schematic of our experimental set-up. The essential features of this apparatus include (1) an adjustable height gauge fitted with a hypodermic needle, (2) a motorized-syringe device, (3) a Redlake MotionPro 10000 Digital High Speed Camera, (4) a high power light source, (5) a platform on the adjustable height gauge

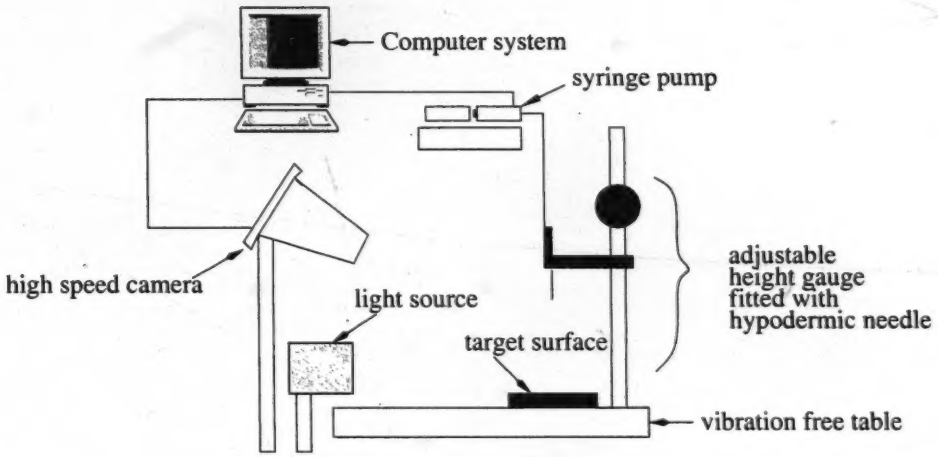

Figure 2.3: Schematic of the experimental set-up

to hold the test piece, and (5) a vibration-free table. In actual experiment, droplets were formed at the tip of a Hamilton (gauge 17) stainless steel needle via a slow motion of a motorized syringe pump, forming pendant drops at the tip of the needle. The drops then fell under their own weight onto the target surfaces (2.5 cm $\times$ 4 cm). Impact velocities were calculated using equations of motion $U = \sqrt{2gh}$, where g and h are the acceleration of gravity and height of droplet released, respectively. These values were subsequently used to compute the impact energy, as characterized by the Weber number. We started recording the motion process while the droplet was at a distance of $\approx$ 15 mm above the test surface up to the entire recoil of the resulting thin film. The camera is capable of recording at a maximum of 10,000 frames per second. For recording the impact on $HS(CH_2)_{17}CH_3$ monolayer, the camera was adjusted approximately perpendicular to the target surface and was placed at a distance of about 15 inches away from the test piece. In the case of $HS(CH_2)_{15}CO_2H$, the angle of inclination of the camera was approximately $30 - 36°$. It was observed that this angle of inclination provides the optimal view of collision dynamics as water droplets

wet the surface of $HS(CH_2)_{15}CO_2H$ very quickly upon collision. This arrangement does not affect the measurements taken in this study as the spreading dynamics was clearly in focus for all the surfaces at the chosen settings.

For the impacting experiments, images were taken at 2,500 frames per second with an arbitrary chosen resolution of 128 × 128 which results in an exposure time of 394 μs, standard shutter of 1/2500 μs and a total recording time of 52.365 s; while a resolution of 256 × 204 yielded an exposure time of 394 μs and a total recording time of 16.428 s. At a higher impact energy, a reasonable shutter speed at the selected resolution was found to be 1/7500 μs. This provides a reduced exposure time of 132 μs. For the $HS(CH_2)_{17}CH_3$ surface, there is appreciable rebound after reaching the maximum diameter (see later) and hence the need for a zero angle of inclination for the camera. However, the dynamic advancing angles of the droplets on the $HS(CH_2)_{15}CO_2H$ is practically less than 15°, necessitating a higher angle of incline for improved clarity. Adequate illumination was also necessary for this recording. A 1 kW Lowel DP high power floodlight was used for background illumination, so that there is sufficient reflection to record the resulting dynamical processes. In addition, all experiments were conducted at night to ensure that vibrations were highly reduced.

The diameter of the droplet was determined by a weight measurement technique. Several droplets were weighted with the aid of a high-precision balance (Explorer OHAUS) and a mean value was obtained. The droplet diameter was determined by assuming them to be perfectly spherical. The wetted diameters of the droplets at each frame was obtained using a MiDAS software from the MotionPro camera system. Rather than using a different object for calibration, the original diameter of the droplet in each frame prior to landing on the surface was measured and stored as the reference. The system measures the temporal dimensions of the spreading film by direct conversion from the number of pixels. Alternatively, the dimensions could be

determined in pixels uniformly and divided by the pixel size of the original diameter. The results obtained by these two methods were similar.

2.2.6 Characterization of SAMs

The procedures for characterization of SAMs are similar to those by Yang et al [60]. SAMs were first characterized by a Sopra GESP-5 variable angle spectroscopic ellipsometer. The ellipsometry measurements were performed with the aid of a rotating polarizer in the tracking analyzer mode. A broad band of light (300–850 nm) from a 75 W Xe-arc lamp is linearly polarized and directed onto the film surface at an incident angle of 75° from the surface normal. The $\tan\Psi$ and $\cos\Delta$ for each bare gold substrate were measured as references after evaporation. After immersion of the substrates into ethanol solutions of octadecanethiol and 16-mercaptohexadecanoic acid, the $\tan\Psi$ and $\cos\Delta$ were again measured using an ambient-film substrate model for regression with known refractive indices (n and k) for octadecanethiol and 16-mercaptohexadecanoic acid adsorbed onto gold. Rather than assuming an index of refraction (e.g., $n = 1.46$) at a given wavelength of, say, $\lambda = 632.8$ nm, the refractive index for both monolayers adsorbed onto gold as a function of the wavelength were independently obtained from a Sopra GXR grazing reflectometer. The thickness of the adsorbed monolayers were computed using the formula:

$$(tan\Psi)e^{i\Delta} = f(n_i k_i T_i), \tag{2.1}$$

where n and k are the spatial constants of the film, T is its thickness and the subscript i represents different wavelengths.

Fourier Transform Infrared (FT-IR) characterization of the surfaces were performed using a Nitrogen-purged Nexus 670 spectrometer with a KBr (Potassium-

Table 2.1: Impact velocities and other dimensionless parameters for water droplets ($D_0 = 3.6280$ mm).

Impact velocity, U (m/s)	We	Re
0.8646	37	3103
1.0936	60	3925
1.2628	79	4533
3.0570	466	10972

Bromide) beam splitter and liquid Nitrogen-cooled MCT (Mercury-Cadmium-Telluride) detector. The range of the detectable signals is 7400−600 cm^{-1}. Optimal parameters were set for all the surfaces: for the octadecanethiol monolayers, the gain was to 8 with a resolution of 2 cm^{-1} and 256 scans; the gain for the 16-mercaptohexadecanoic acid and the mixed SAMs was set to 8 with a resolution to 4 cm^{-1} and 512 scans. The aperture was set to 32 in for each measurement. The spectra displayed in this paper has been baseline-corrected for better clarity.

Atomic force microscopy (AFM) measurements were performed using a Digital Instruments Nanoscope IIIa atomic force microscope (Digital Instruments, Santa Barbara, CA). Standard silicon nitride cantilevered probes were used with a force/spring constant in the range between 0.06 and 0.58 N/m. The surfaces were cut into approximately 1 cm × 1 cm samples to fit onto a 1.5 cm × 1.5 cm sample stage.

2.2.7 Parameters for Impact

For the impacting experiments, water droplets were employed for 4 impact velocities. The resulting dimensionless numbers are given in Table 2.1. Their corresponding Weber number values were 37, 60, 79, and 466. All experiments were performed under laboratory conditions.

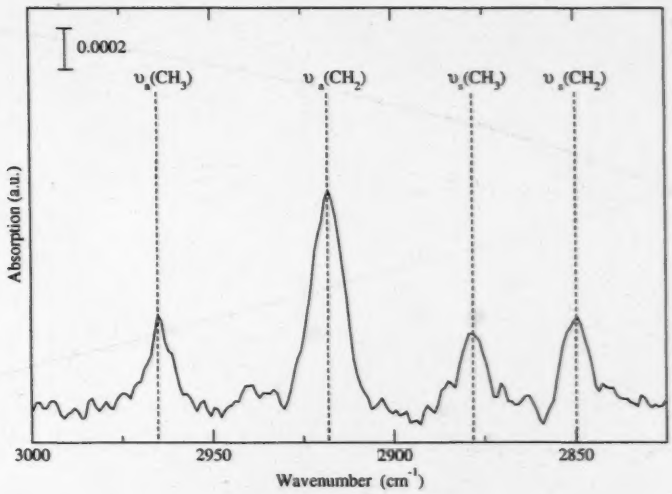

Figure 2.4: FT-IR spectra of $Au/S(CH_2)_{17}CH_3$

2.3 Results and Discussion

2.3.1 Surface Characterization by FT-IR, AFM, Ellipsometer and Contact angle

Infrared Measurements. Fourier Transform Infrared (FT-IR) characterization of the surfaces were performed using a Nitrogen-purged Nexus 670 spectrometer with a KBr (Potassium-Bromide) beam splitter and liquid Nitrogen-cooled MCT (Mercury-Cadmium-Telluride) detector. For simplicity, we used CH_3 to represent $HS(CH_2)_{17}CH_3$ surface and CO_2H for $HS(CH_2)_{15}CO_2H$. Figure 2.4 shows the FT-IR spectra for the CH_3 monolayer. The results reflect the anticipated peak positions for the symmetric $\nu_s(CH_2)$ and asymmetric $\nu_a(CH_2)$ stretching at 2918 cm^{-1} and 2850 cm^{-1}, respectively. The figure also shows the peaks for the symmetric $\nu_s(CH_3)$ and asymmetric methyl groups $\nu_a(CH_3)$ at 2963 cm^{-1} and 2878 cm^{-1}, respectively, suggesting that the surfaces are well-packed with a polycrystalline structure.

The FT-IR result for CO_2H are displayed in Figure 2.5. Typical absorption band

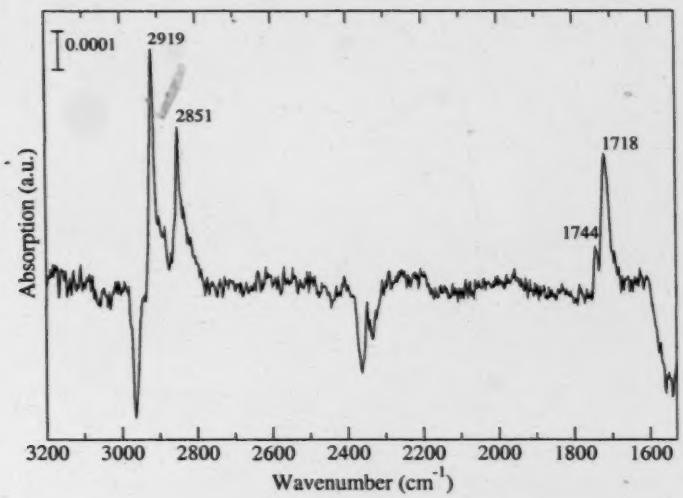

Figure 2.5: FT-IR spectra of $Au/S(CH_2)_{15}CO_2H$

spectra for O−H component of the carboxylic acid lies in the wavenumber range of 3300–2500 cm^{-1}; the C=O double bond stretching in the range between 1760 – 1665 cm^{-1}. This expectation is met in our measurements. It is evident that both the CH_3 and CO_2H surfaces are chemically different, although their thickness differ by only $\sim$ 2 Å.

Spectroscopic Ellipsometry. Ellipsometric studies were used to characterize the thickness of the surfaces using a Sopra GESP-5 variable angle ellipsometer. The results of our measurements were 20.4 Å and 18.3 Å for CH_3 and CO_2H surfaces, respectively; they agree with the expectation that the two surfaces differ only by the exterior terminal groups. Such results are also consistent with those reported in the literature [60, 61].

Atomic Force Microscopy. The AFM images for the CH_3 and CO_2H monolayers are shown in Figures 2.6 and 2.7, respectively. It can be seen that the mean surface

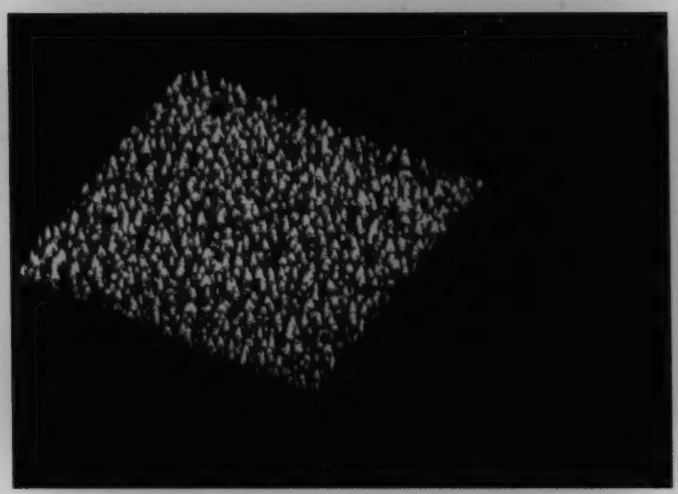

Figure 2.6: 3-D AFM image of $Au/S(CH_2)_{17}CH_3$ surface

roughness of the CH_3 and CO_2H surfaces are 2.016 nm and 1.058 nm, respectively. It has been found [62] that this degree of surface roughness has no influence on the phenomenological wetting characteristics in terms of solid surface tensions. Thus, we expect that the difference in the collision dynamics of water on the CH_3 and CO_2H surfaces are due exclusively to solid surface tensions with minimal effect from surface roughness.

Contact angle characterization. Although a systematic study of surface energetics in terms of contact angle poses some fundamental difficulty when there is a possibility of complex and unidentifiable penetration of the liquid on the SAMs [16], it is nonetheless possible to account for differential wettabilities in terms of these phenomenological contact angle data for the surfaces we have generated in our experiments. Following the general procedures described in [16] for axisymmetric drop shape analysis, the contact angles of 119.1° [60] has been calculated for the CH_3 and is normally estimated as $\sim 15°$ for CO_2H surfaces.

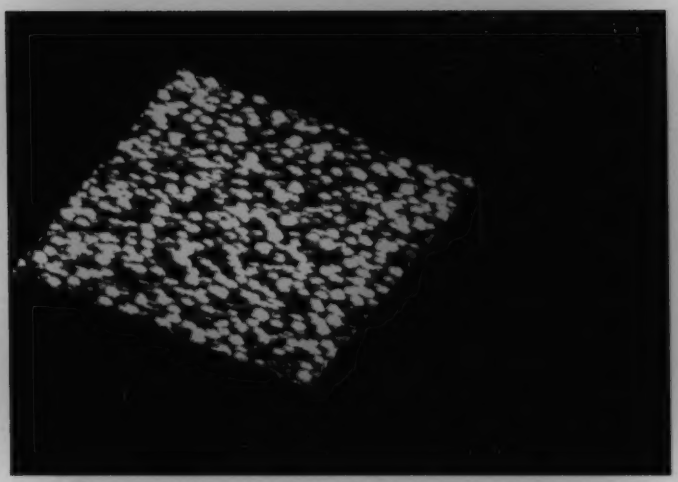

Figure 2.7: 3-D AFM image of $Au/S(CH_2)_{15}CO_2H$ surface

2.3.2 Observation of spreading phenomenon

Observation of the drop impact dynamics offers interesting physical evidence that surface energetics plays an important role in the collision dynamics of droplets on the tailored surfaces. Table 2.2 shows sequence of pictures for water droplet impact onto the $Au/S(CH_2)_{17}CH_3$ and $Au/S(CH_2)_{15}CO_2H$ monolayers for two Weber numbers: 37 and 60. The photographs for We = 79 and We = 466 reveal similar qualitative trends.

We note that the initial phases of collision dynamics for all the surfaces are similar: a very thin liquid film jets out radially from the point of contact with the solid surface after impact. This behavior has been attributed to a sudden rise in pressure occasioned by the abrupt impedance to the droplet flight [63]. The observed thin film spreads out with a speed u_e which is considerably greater than the impact velocity U. A full account of this dynamics may be found in the theory by Lesser [21]. The sudden rise in pressure results in a shock wave which propagates upward into the

drop, causing droplet compression. The pressure rise is, however, relieved only by the film spread into a radial direction, assuming the shape of a distorted flattened disc. Similar observations were also made by Chandra and Avedisian [11].

The increase in the spreading ratio with time for all the Weber numbers considered is a reflection of the role of inertia in controlling droplet spread. At a higher impact energy, surface effects and viscous dissipation tend to be overcome by droplet inertia. This is shown by the results in Figure 2.8 where the normalized maximum spreading diameter is plotted against the Weber number. Since droplet spread on the CO_2H surface is generally greater than on the CH_3 surface, we used the former as the basis for comparison. It is observed that the ratio $D_{max(CH_3)}/D_{max(CO_2H)}$ tends toward unity as the Weber number approaches infinity. While intermolecular forces resulting from droplet-surface interaction play a vital role in droplet spreading, its effect is highly reduced in the presence of a dominating force for one and the same solid surface.

The hydrophobicity of the CH_3 surfaces are evident in the lower spread and violent rebound after spreading to the maximum diameter. This results from the repulsive intermolecular forces between water molecules and the hydrophobic tail groups of CH_3 monolayer. Thus, after reaching the maximum diameter, the film retracts from the wetted portion of the surface and undergoes rapid rebound and oscillations in an attempt to reduce its exposure to the solid surface. The rebound is observed to be more pronounced at higher impact Weber numbers. The height of rebound was observed to be proportional to the impact energy of the droplet. At We = 60 and 79, droplet recoil velocity was so high that axial rebound resulted in the detachment of a large portion of the parent (preimpact) droplet. Secondary droplets detachment was also observed to increase with increasing impact energy. This observation is typified for the impact at We = 466: after recoil, the droplet stretches vertically upward and the wetted area reduces far below from the original diameter before impact. The

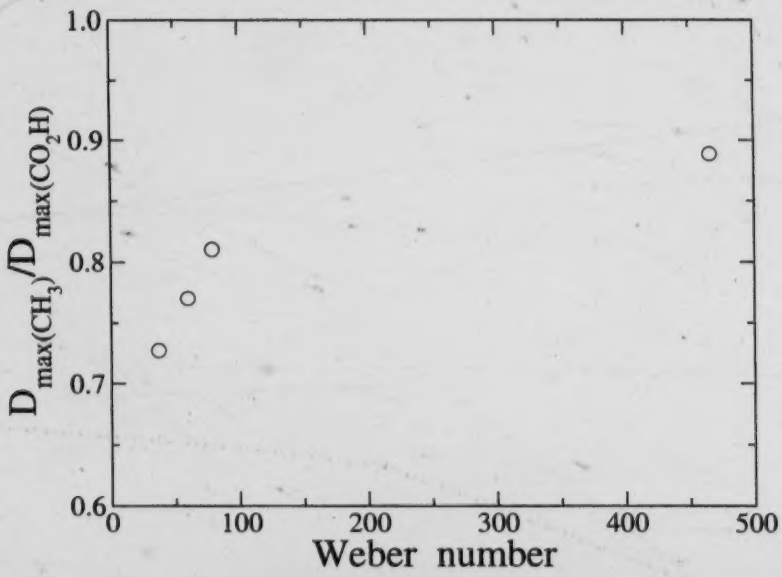

Figure 2.8: Ratio of the maximum spreading diameter of CH_3 $D_{max(CH_3)}$ to that of CO_2H $D_{max(CO_2H)}$ versus the impact Weber number. The effect of inertia is shown to dominate surface tension effect as the impact Weber number increases.

impact on CO_2H contrasts this behavior as the droplets spread uniformly and are literally bound to the surface.

For the same Weber number, the spreading ratio $\beta(t)$ of drop impact on the CO_2H monolayer is observed to be higher than that on the CH_3 monolayer (see Table 2.2). Of course, this is to be expected, given that the solid surface wettabilities also follow similar patterns. To account for this, we first review the account by Bowden and Field [64]. They suggested that, after drop impact and the subsequent formation of the shock wave due to pressure rise, the film contact edge proceeds outward with a velocity u_e which is supersonic with respect to the speed of sound in the drop and those of dilational and shear waves in the solid wall. The relation between the impact

velocity U, outspreading edge velocity u_e and contact angle θ is given by [39]

$$u_e = \frac{U}{\tan\theta} \tag{2.2}$$

From Eq.(2.2), the smaller the contact angle $\theta(t)$ (which we may call the dynamic advancing angle), the higher the contact edge velocity (and hence, film spread velocity u_e). It is well known that our CO_2H surface has a higher solid surface tension and hence enhanced water wettability when compared to the surfaces of CH_3. Thus, a smaller water contact angle is implied for the CO_2H surface. This result is consistent with that in Ref. [65] where the equilibrium contact angles of water are known to be typically less than 15° for the high energy CO_2H surfaces. But the contact angle of the CH_3 is about 119°. Similar wetting properties also characterize the physics of the dynamic situation as shown in Table 2.2. These observations also show that, for different solid surfaces, solid surface tension (surface energetics) has a significant effect on impact dynamics. Contrary to an earlier observation [39], we observed that $\beta(t)$ is progressively higher (at least during the first 2.4 ms) for the more energetic CO_2H surface. Unlike the dynamics on the CH_3 monolayer, the droplet remained pinned to the CO_2H surface after reaching its maximum diameter. This is the result of strong attractive intermolecular interactions between the end CO_2H tail group and the water molecules. These interactions manifest themselves as a strong adhesion force between the water and the CO_2H surface. Thus, a higher solid surface tension significantly inhibits droplet rebound. This has the similar effect as adding surfactant to impacting liquid for reducing droplet rebound, and possibly, splashing. Our results for CO_2H surfaces also indicate that there is a wave that travels back and forth from the edge of the droplets; nevertheless, the change from the maximum diameter appear to be insignificant. Typically, a thin film at the periphery of the splat

remains attached to the solid surface while circular rings in the inner region move back and forth at an attempted retraction sequence. The resistance to this recoil motion due to strong droplet-surface interaction results in a wavy motion within the droplet. Here, we observed that droplet recoil is more sensitive to solid surface tensions. A more quantitative view may be necessary; thus, a rough estimate of the thermodynamic work of adhesion for the CH_3 and CO_2H surfaces are 37.3 and 142.9 mJ/m^2, respectively [66, 67]. We see that the work of adhesion W_{sl} increases as the contact angle (and hence hydrophobicity) decreases. A more quantitative study of the effect of the work of adhesion will be investigated in Chapters 3 and 4.

2.3.3 Surface wettability and model predictions

Several methods are available to quantify the dependence of spreading ratio β with time. Some of these models are purely empirical or semi-empirical, matching only the author's experimental data. Since we have carefully characterized our solid surfaces using several surface analytical techniques, it is believed that the data we obtained reflect purely solid surface tension effects. Thus, comparing these data with some literature models might provide evidence as to whether the physics of the impacting droplets spreading and recoil have been fully accounted for by the selected models. A brief review of some of these models will be discussed below.

Loehr [68] proposed a model that was consistent with his experimental results as $\beta(\tau) = 1 - \exp(-c\tau)$, where $\tau = tU/R$ is the normalized time, R is the drop radius and c is a nondimensional parameter that may still be a function of the liquid surface tension. The yet-to-be defined parameter c places a limitation on its use. Kim et al. [40] employed variational methods together with a cylindrical model of the spreading

droplets to determine the time-varying base diameter in the form

$$D_b = [D_{max}^2 - \frac{4}{3}k(t - t_i)]^{1/2}, \tag{2.3}$$

where D_{max} is the maximum base diameter at $t = t_i$ and θ is the contact angle. The parameter k is defined as

$$k = 2(1 - \cos\theta)/\psi \tag{2.4}$$

where ψ was given by $\psi = (\beta \cdot \mathrm{Oh})$. Oh is the Ohnesorge number given as

$$\mathrm{Oh} = \mu/(\rho D \lambda_{lv})^{1/2} \tag{2.5}$$

and β can be obtained from

$$\beta = F_d/\mathrm{Oh}^{1/2} \tag{2.6}$$

Finally, F_d is a dissipation factor which was introduced as an empirical constant in scaling the viscous stresses in the model. However, the value of F_d can only be determined by experiments or computation. In an experimental study, Manzello et al. [37] compared their results with the models by Bolle and Moreau [10] and Shi and Chen [46]. The former gives the time dependence of the spreading film as

$$\beta(t) = 1.67[3.1\tau - \tau^2] \tag{2.7}$$

where τ is the dimensionless time equals to tU/D; the latter proposed two models depending on whether the droplet wets the surface or not. We have selected the model that best predicts our experimental data. Their model for the temporal evolution of

the liquid film diameter was given as

$$D(t) = 1.6U\left[t - \frac{6.8\gamma_{lv}}{\rho D^3}U^{0.25}t^{2.95}\right] + D \tag{2.8}$$

In their comparison, Manzello et al. [37] reported that the latter was in better agreement with their experimental data for predicting $\beta(t)$, and attributed that success to the fact that the model incorporated liquid fluid properties.

In this chapter, we have selected two models for comparison of their prediction and with our experimental data. The first is the semi-empirical model by Shi and Chen [46] given above and another, a more recent analytical one, by Roisman et al. [59]. These models have been selected because they do not require the use of additional adjustable constants. The former models the spreading history up to the point before droplet recoil commences, while the second model accounts for both the spreading and recoil stages. For comparison purpose, we express Eq.(2.8) in terms of the spreading ratio β as follows

$$\beta(t) = \frac{D(t)}{D} = 1.6\frac{U}{D}\left[t - \frac{6.8\gamma_{lv}}{\rho D^3}U^{0.25}t^{2.95}\right] + 1 \tag{2.9}$$

The model for time dependent spread film evolution developed in Ref. [59] in their equation (14.3) is given as

$$\bar{R}_r = C(\bar{t} + \bar{\tau}) - \sqrt{\frac{1 - \cos\langle\theta\rangle}{\bar{\eta}We}}(\bar{t} + \bar{\tau})^2. \tag{2.10}$$

where C is a constant of integration, found from the initial condition given that $\bar{R}_r$=$1/2\bar{D}_1$ when $\bar{t} = 1$. For this condition,

$$C = \frac{\bar{D}_1}{2}\left[\sqrt{\frac{6(1 - \cos\langle\theta\rangle)}{We}} + \frac{1}{1 + \bar{\tau}}\right] \tag{2.11}$$

In Eqs.(2.10) and (2.11), $\bar{t}$ is dimensionless time, θ is the average value of the dynamic contact angle, which is calculated using Hoffman's law [69]:

$$\theta = f_{Hoff}\Big(Ca + f_{Hoff}^{-1}(\theta_0)\Big), \tag{2.12}$$

where $f_{Hoff}^{-1}(\cdot)$ is the inverse function of $f_{Hoff}(\cdot)$ defined by

$$f_{Hoff}(x) = \arccos\left(1 - 2\tanh\left[5.16(\frac{x}{1+1.31x^{0.99}})^{0.706}\right]\right) \tag{2.13}$$

In Eq.(2.12), θ_0 is the static contact angle. The authors assumed that the capillary number of the spreading film may be computed by equating the velocity of propagation to the impact velocity, i.e, $Ca \approx \mu U/\gamma_{lv}$. The remaining terms are given as:

$$\bar{\eta} = \bar{h}_1(1+\bar{\tau})^2 \tag{2.14}$$

and,

$$\bar{\tau} = \frac{\bar{D}_1}{4\sqrt{6}}\left[\frac{1}{12} + \frac{1}{We} - \frac{1}{Re}(\frac{1}{20\bar{h}_1^3} + \frac{3}{5\bar{h}_1}) - \frac{\bar{D}^2}{4We}(1-\cos\langle\theta\rangle) - \frac{\bar{D}_1\bar{h}_1}{We}\right]^{-1/2} - 1. \tag{2.15}$$

$\bar{h}_1$ and $\bar{D}_1$ are, respectively, the droplet thickness and diameter at the instant when the dimensionless time $\bar{t} \approx 1$. They are related by the following respective equations [Eqs.(3.14) and (3.15) in Ref.[59]]:

$$3We + 5(1-\cos\langle\theta\rangle)Re\cdot\bar{h}_1 = 10Re\cdot We\cdot\bar{h}_1^3 \tag{2.16}$$

$$\bar{D}_1 = \frac{D_1}{D} = \sqrt{\frac{2}{3\bar{h}_1}}. \tag{2.17}$$

Displayed in Figure 2.9 are the comparison of our experimental results with those

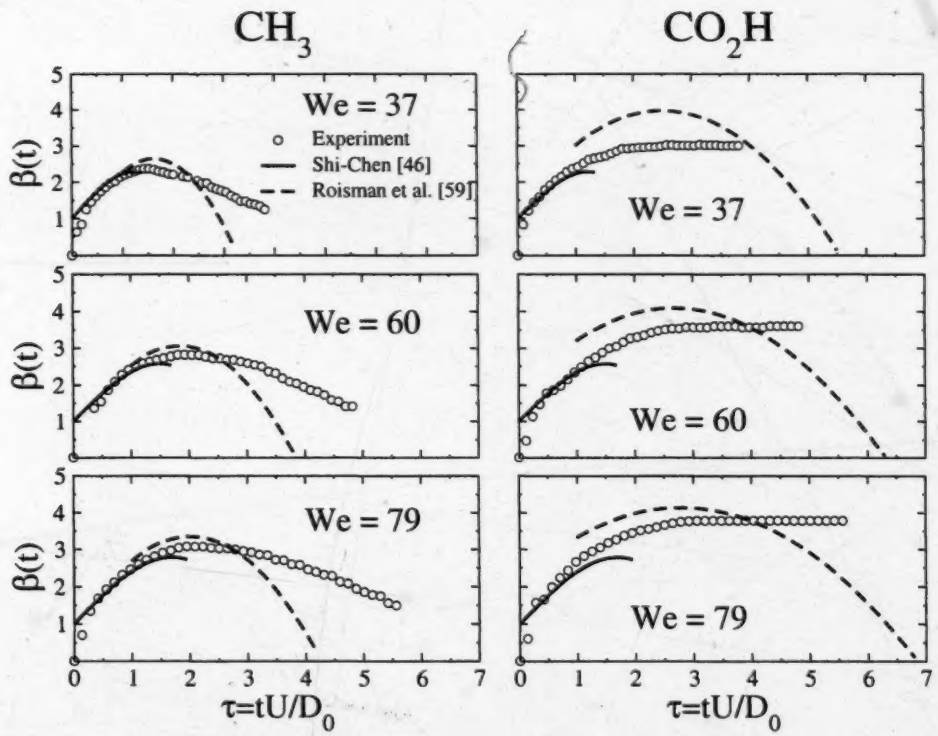

Figure 2.9: Time evolution of spreading factor $\beta(t)$ of water impacting onto the CH_3 and CO_2H surfaces.

from the models of Shi and Chen [46] and Roisman et al [59] for $We = 37$, 60 and 79. Since the time evolution of the spreading predicted by Shi and Chen's model does not include the recoil phase, we have presented the data up to the time just after attaining the maximum spread diameter. As expected, the first model predicts the spreading behavior of water droplet impact on all the surfaces to be the same; while those of the experimental data are markedly different. This is because the model has excluded the effect of solid surface tensions on droplet impact dynamics explicitly. Although the model prediction contains no information to account for solid-liquid interactions, it, nonetheless, shares similar qualitative trend with the data curve. For example, at $We = 79$, the model shares similar trend with our data for dimensionless time

up to $\tau \approx 1.5$, In all the cases, however, the maximum spreading factor is generally under-predicted, and this is even more so for the CO_2H. Moreover, the model did not account for the spreading ratio at the time just before impact $D(t) = 0$. When we consider these results in dimensional time scale, we note that Shi and Chen's model, although simple and empirical, offers a reasonable prediction for all surfaces within 0.5ms $\leqslant$ t $\leqslant$ 5ms. This might suggest the dominating influence of inertia during this period. It is interesting to observe that this dominant influence of inertia was important for these two chemically different surfaces. The effect of the specific solid-liquid interactions becomes more important as inertial effects starts to diminish beyond the first 5 ms and this is where the two model fail badly.

Also included in Figure 2.9 are the plots for the model by Roisman et al. [59]. As mentioned earlier, their model accounts for differential energetics via the dynamic contact angle using the Hoffman's law. The model prediction is only valid from $\tau =$ 1 onwards. In most cases, the model significantly over-predicts the spreading factors by a greater margin than the first model. In addition, the model by Roisman et al. [59] predicts the collision dynamics with very sharp retraction phases.

In order to observe the performance of these models in predicting the possible, or anticipated, dominance of inertial over solid-liquid interaction and liquid-fluid surface tension effects, the models were also compared with the experimental results for a higher Weber number, $We = 466$, as shown in Figure 2.10. The model by Shi and Chen [46] predicts the spreading trend relatively well up to $\tau \approx 3.5$. The error in computing the maximum spreading ratio was much lower compared to those from smaller weber numbers, implying that the model conforms to physical reality. Results for the Roisman et al [59] model could not be computed for the CO_2H surface because the term $\bar{\tau}$ in Eq.(2.15) results in a complex square root.

Since the model by Shi and Chen [46] does predict our experimental data more

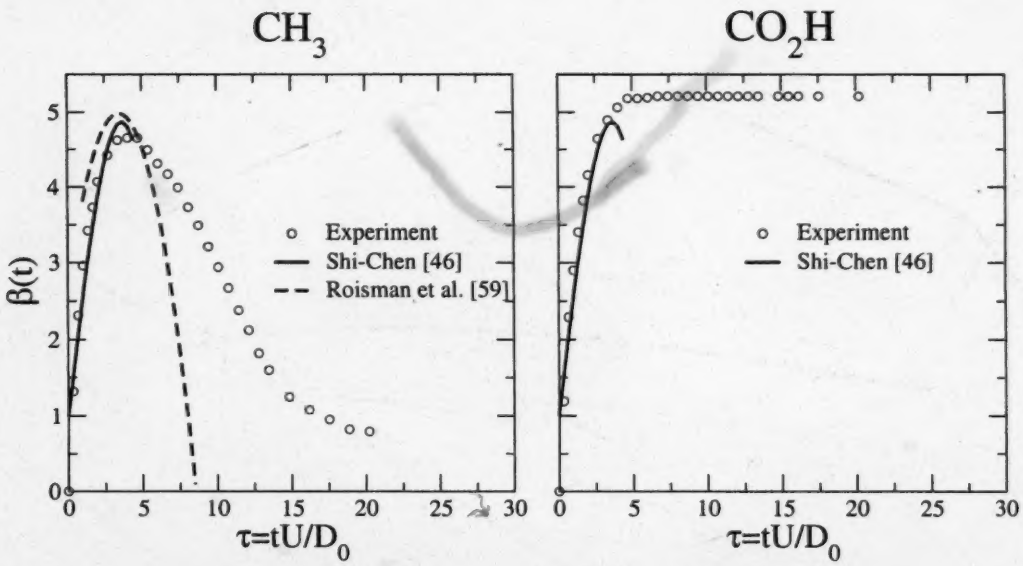

Figure 2.10: Time evolution of spread factors of water on impact at $We = 466$ on CH_3 and CO_2H surfaces. Results for the Roisman et al [59] model could not be computed for the CO_2H surface because the term $\bar{\tau}$ in Eq.(2.15) results in a complex square root.

closely, it may be worthwhile to examine the physics of the model, with a view to account for its failure in taking different solid surface properties into consideration. The model, like several others of its kind, utilizes the energy conservation principle applied in the Lagrangian form to the spreading droplet mass (which approximates the shape of a disc) [Eq.(3) in Ref.[46]]:

$$\delta(E_k + E_p + E_D) = 0, \tag{2.18}$$

The first term in the bracket represents the total kinetic energy of the droplet; the second term the total surface potential energy; and the third, the accumulated dissipation energy due to viscous motion within the liquid mass. In calculating the temporal evolution of the kinetic energy terms as droplet spread on surfaces, an impact coefficient, ξ, was employed to measure the energy consumed during initial

deformation stage in their Eqs.(1) and (2):

$$E_{k1} = \xi E_{k_i} \tag{2.19}$$

$$\xi = \exp(-0.083U^{1.5}) \tag{2.20}$$

where E_{k_i} and E_{k1} are the total kinetic energy of the initial incoming droplet and the kinetic energy of the initial spreading disc, respectively. By fitting the experimental data of Toda [70] for the maximum spreading radii, Shi and Chen [46] were able to obtain Eq.(2.20) for ξ. It should be noted that the experimental data from Toda's work used glass surface as the substrate at room temperature. However, it is anticipated that the coefficients in Eq.(2.20) would differ if the maximum spreading data from a different substrate (with different solid surface tension, or wettability) were used. Ignoring the solid surface property then results in the failure to adequately account for the maximum spread on surfaces with higher surface energetics.

Be that as it may, our results obtained here have important implication on literature spreading dynamic data on surfaces which are less well-prepared and characterized. As a matter of fact, we have shown that small variation of chemical functionality ($\sim$ 2 Å) can cause the water droplet impact dynamics to be substantially different. As adsorption of contaminants (hydrocarbons) on high energy surfaces occurs readily under ambient condition, interpretation of impact dynamic data on such surfaces can be complicated. The surfaces of interest might have been chemically changed due to, e.g, physiochemical adsorption. When this happens, models that are empirical or semi-empirical would have deduced a relationship that reflects the changed energetics, rather than that of the original unchanged substrates. and a systematic study of the effect of surface energetics on impact dynamics of droplets would not have been possible. Thus, understanding the underlying physics of droplet dynamics on surfaces

calls for experiments that characterize solid surfaces carefully.

2.4 Conclusions

We have studied experimentally the effects of tailored surface energetics on the collision dynamics of a 3.6280 mm diameter water droplet impact by means of well-characterized self-assembled monolayers (SAMs) of $Au/S(CH_2)_{17}CH_3$ and $Au/S(CH_2)_{15}CO_2H$. The SAMs surfaces were examined by means a Fourier Transform-Infrared Spectroscopy (FT-IR), Variable Angle Spectroscopy Ellipsometry (VASE) Atomic Force Microscopy (AFM) and Axisymmetric Drop Shape Analysis - Profile technique for its chemical functionality, thickness, roughness and contact angle, respectively. Their surface qualities are so good that surface roughness is on the order of less than 2 nm which is known to have little effect on the wetting characteristics. The observed difference in the collision dynamics is expected to be due exclusively to solid surface energetics. In addition, we observe that wettability characterization alone may not serve to completely explain some solid-liquid interactions.

Our results indicate that droplet fluid inertia tend to dominate the effect of solid-liquid interaction even for surfaces with widely different wettabilities. This dominance is, however, only limited to the maximum extent of spread — that is, the difference in the maximum spreading ratio for all surfaces decreases with increasing impact energy. The retraction phase still retains similar characteristics of the solid-liquid adhesion strength as for the lower Weber number impacts: droplet rebounds for the hydrophobic $Au/S(CH_2)_{17}CH_3$ surface, while the droplet stays bound at the solid surface for the more energetic $Au/S(CH_2)_{15}CO_2H$ surface.

We have also compared our experimental data with two models that predict the time evolution of droplet spread: (1) an older semi-empirical model by Shi and Chen [46] which utilizes the variational principle; and, (2) a more recent analytical one

by Roisman et al [59] which solves the mass and momentum equations to derive an analytical expression for both the maximum spread diameter and the time-varying spread factor. The first model, although based on empirical correlation, predicts our experimental results more accurately on the initial spreading behavior than the latter.

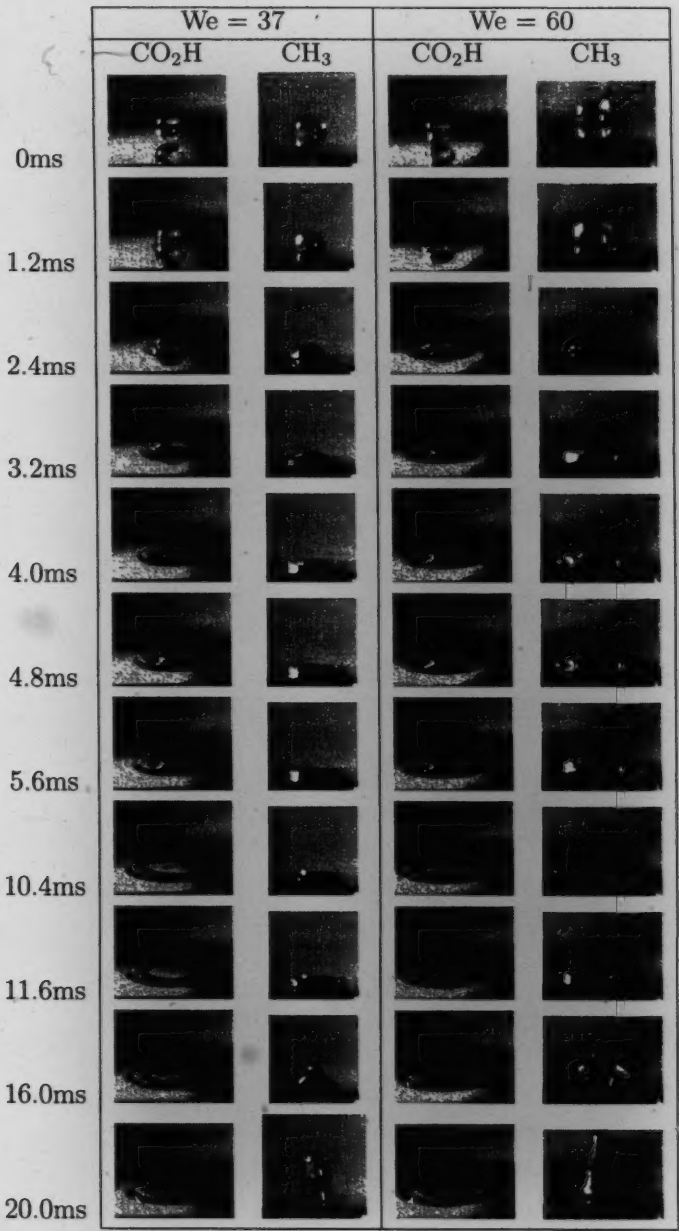

Table 2.2: Sequential images of the impacting water droplets onto the $Au/S(CH_2)_{15}CO_2H$ (CO_2H) and $Au/S(CH_2)_{17}CH_3$ (CH_3) surfaces at different temporal resolutions for two Weber numbers, 37 and 60.

CHAPTER 3

PREDICTING THE MAXIMUM SPREADING DIAMETER

3.1 Introduction

It was mentioned earlier that the impact of liquid droplets on solid surfaces results in several outcomes, including spreading, recoil, and splashing of the droplets. One of the most important parameters of interest in the study of drop impact dynamics remains the maximum spreading diameter D_{max}. It is often normalized by the original diameter of the droplet prior to impact, resulting in the maximum spreading ratio β_{max}. The ability to accurately predict the maximum spreading factor is fundamental to optimizing several practical — and industrial — application. For example, the cooling effectiveness of impacting droplets relies on the area wetted by the impacting liquid on the hot surfaces and the rate at which the droplets leave the wetted area. It is therefore important that β_{max} be determined correctly since the wetted area is of the order of β_{max}^2. β_{max} has been determined independently by several authors using various numerical methods and commercial softwares which incorporates some specialized interface tracking schemes to model the deforming liquid interface. Others have computed β_{max} using energy conservation techniques with consideration of the

pre-impact and final stages of impacting droplets dynamics. In this chapter, we examine the second group of models, largely because of the simplicity with which they can be used to quickly investigate the wetting effect of impacting droplets. Apart from that, they do not require as much computing power as numerical schemes.

While the development of a simple model based on energy conservation principle seems to be a viable option, several published models present conflicting reports on the physical parameters that contribute towards the determination of β_{max}, especially with respect to surface energy and viscous energy dissipation. The work of Bennet and Poulikakos [24] investigated some of these models for predicting β_{max} where four models were selected from Refs. [11, 23, 43, 45], respectively. It was concluded that the last two were inadequate in predicting β_{max} due to over-simplifications in accounting for factors that affect droplet dynamics. The model by Madejski [23] was then employed for improvement as Bennet and Poulikakos believed that such a model provides best estimate for the viscous energy dissipation term in terms of surface energy. The central focus of their study was the relative importance of the effect of surface tension and viscous energy dissipation in terminating the spread of liquid droplet during splat-quench solidification process, and hence, in determining the maximum spreading factor β_{max}. A similar study by Healy et al. [42] considered 7 model predictions and compared them with experimental data from the literature. Two models (Refs. [11, 23]) from the work of Bennet and Poulikakos and four others were selected. It was concluded that the Kurabayashi-Yang model [71] provided the best estimate of the experimental data for β_{max} based on error analysis.

Apart from those considered above, some other models have also been proposed recently. The model by Pasandideh-Fard et al [29] was an improvement on the model by Chandra and Avedisian [11]. Kim and Chun [40] implemented conservation of energy and variational principle to develop differential equations for the time-varying

diameter and height of droplet during spread. Their work incorporated a dissipation factor which was introduced as an empirical constant in scaling the viscous stresses in the model. However, the value of this dissipation factor can only be determined by experiments or computation and, therefore, will not be considered in our work here.

One of the most recent models with regard to the spreading ratio is due to Roisman et al. [59] considered in Chapter 2. In addition to deriving an equation for time evolution of spreading factor (or ratio), they also obtained an approximate expression for β_{max}. The model predictions were compared with experimental data from the literature. It was concluded that such a model performed best in predicting β_{max} at lowest and relatively high velocities. For velocities outside this range, a relative error of approximately 20% was obtained.

This chapter investigates some of the models for predicting β_{max} using carefully controlled experimental procedures. Droplet impact experiments of two liquids (water and formamide) are performed on three carefully prepared solid surfaces that have been rigorously investigated and whose solid surface energetics and wettability are known. The experiment involves the impact of water and formamide droplets at the velocity range of 0.7059 m/s – 2.7932 m/s on poly(methyl methacrylate) PMMA, poly(methyl methacrylate/*n*-butyl methacrylate) P(MMA/*n*BMA), and poly(*n*-butyl methacrylate) P(*n*BMA). Models in the literature are then compared with respect to the relative mean error together with the standard deviation. A modification is made on one of the selected models; the prediction of β_{max} from this modified model is shown to agree well with those from our experiments.

3.2 Method and Materials

Poly(methyl methacrylate) PMMA (cat # 04553, $M_w = 75,000$) in the form of 200 μm beads, poly(*n*-butyl methacrylate) P*n*BMA (cat # 02061) and poly(methyl

methacrylate/*n*-butyl methacrylate) P(MMA/*n*BMA) as fine power (cat # 01922) were purchased from Polysciences (Warrington, P.A.). A 2 % of each polymer/toluene was prepared using toluene (Sigma-Aldrich, 99 + % A.C.C. HPLC grade) as the solvent. Silicon wafers were obtained from Wafer World (West Palm Beach, FL), as test grade in circular discs of about 10 cm diameter. These were then cut into smaller pieces of approximately 3 cm × 5 cm, and were subsequently soaked in chromic acid for at least 24 h, rinsed with deionized ultra filtered (DIUF) water (Fisher Scientific), nitrogen-purged and then dried under a heat lamp before the polymer coating. About one or two drops of the polymer/toluene solution were deposited on the dried silicon wafers inside petri dishes overnight. The solution spreads evenly over the surface and forms a thin layer of the polymer. This method of preparation produced smooth and excellent quality of surfaces, as shown by light fringes as a result of refraction at the surfaces. The implication is that surface roughness is of the order of nanometer or less.

The solid surfaces have been characterized for wettability via contact angle of DIUF water ; density ρ = 0.977 g/cm^3; viscosity μ = 1.01 mPa·s; surface tension γ_{lv} = 72.70 mJ/m^2) and formamide (Aldrich, 99.5+%; ρ = 1.134 g/cm^3; μ = 2.90 mPa·s; γ_{lv} = 59.08 mJ/m^2). The solid surface tensions of the three polymers have been determined from an equation of state approach given by [16, 49, 50, 51] and the results are summarized in Table 3.1.

Liquid droplet for impact was generated by the same method explained in detail in Chapter 2. In this case, however, we also include a gauge 23 for the Hamilton stainless steel needles (in addition to the gauge 17 needle) for the water droplet impact. The droplet produced measured 2.7107 mm. For the formamide droplets, only the gauge 23 needle was used and the droplet measured 2.5296 mm. The diameter of the droplet was determined by the same weight measurement technique described in Chapter 2.

Table 3.1: Summary of the advancing contact angle θ_a and solid-vapor surface tension γ_{sv} from [16] for poly(methyl methacrylate) PMMA, poly(methyl methacrylate/*n*-butyl methacrylate) P(*n*BMA/MMA) and poly(*n*-butyl methacrylate) P*n*BMA

solid surface	liquid	θ_a (degree)	γ_{sv} (mJ/m^2)
Poly(methyl methacrylate) PMMA	water	73.72	39.33
	formamide	57.73	
Poly(methyl methacrylate/ *n*-butyl methacrylate) P(*n*BMA/MMA)	water	81.33	34.59
	formamide	66.33	
Poly(*n*-butyl methacrylate) P*n*BMA	water	90.73	28.71
	formamide	76.41	

Five impact velocities were considered in this study and all experiments were performed under laboratory conditions. The relevant dimensionless numbers as a function of impact velocity are shown in Table 3.2 for water and formamide. The range of impact velocities was selected such that droplets do not break-up upon impact with the solid surface. We have also implemented the same image capture and data analysis technique described in Chapter 2. In order to ensure that the experiments were repeatable and that contaminants were absent from the surface the procedures for cleaning the experimental set-up given in Chapter 2 were also employed. Detailed description of the image capture system for the impacting droplet has been presented previously in Chapter 2 and will not be repeated here for brevity.

3.3 Results and Discussion

3.3.1 Droplet Collision Dynamics

Figure 3.1 displays a series of images for water droplet (D_0 = 2.7107 mm) impacting on PMMA, P(*n*BMA/MMA), and P*n*BMA surfaces at an impact velocity of 0.7059

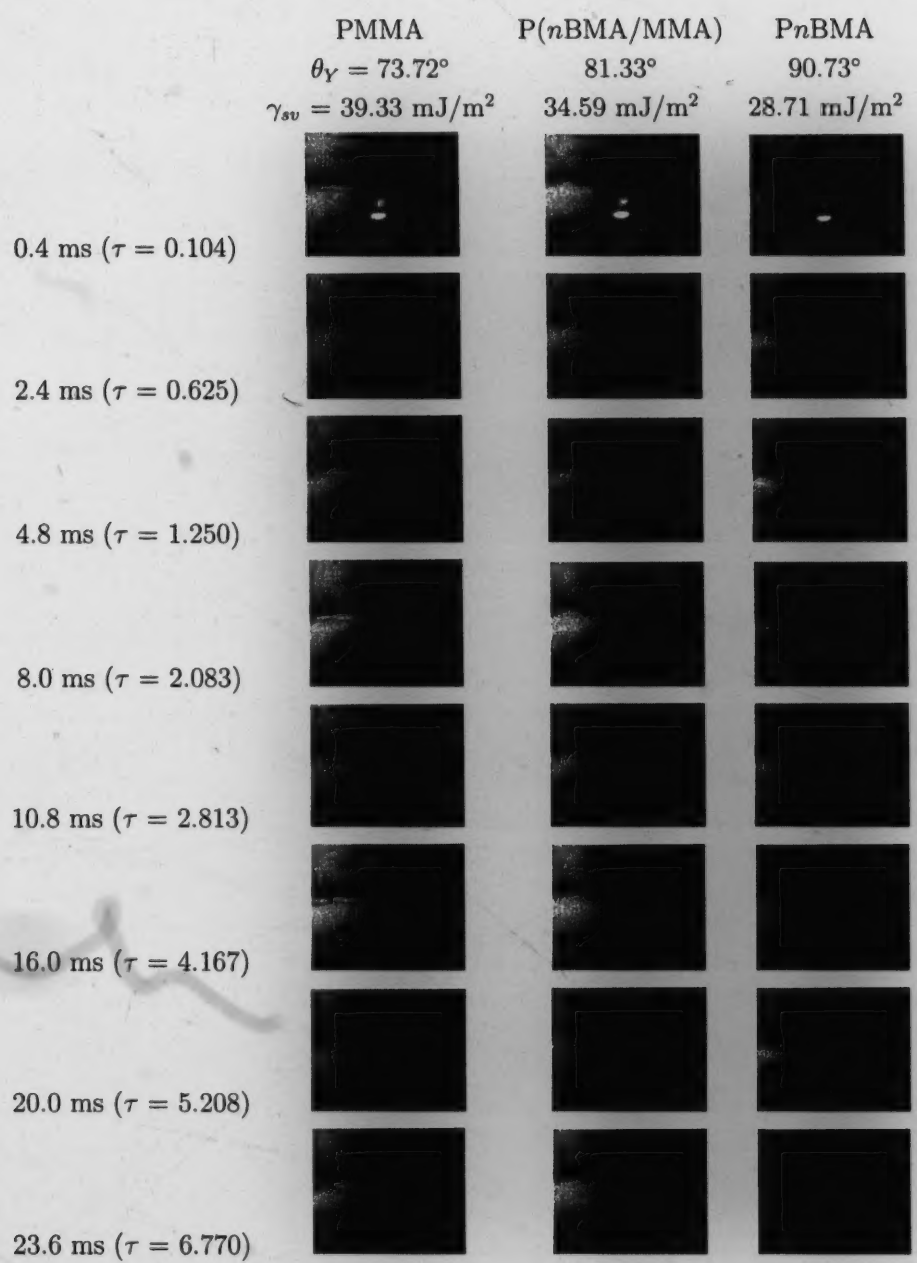

Figure 3.1: Sequential images of a 2.7107 mm water droplet impacting on PMMA, P(nBMA/MMA) and PnBMA surfaces at an impact velocity $U = 0.7059$ m/s. Contact angles θ_Y and solid-vapor surface tensions γ_{sv} were obtained from [16].

Table 3.2: Impact velocities and other dimensionless parameters for water and formamide droplets. D_0 is the initial droplet diameter.

U^*	Water (D_0 = 2.7107 mm)		Water (3.6280 mm)		Formamide (2.5296 mm)	
(m/s)	We	Re	We	Re	We	Re
0.7059	19	1893	25	2534	24	698
1.4119	74	379	99	5068	97	1397
1.8677	130	5009	174	6704	169	1848
2.1178	167	5679	–	–	217	2095
2.7932	–	–	389	10024	–	–

* Velocity of impact

m/s. Apart from the fact that droplet recoils faster in the direction of decreasing solid surface tension PMMA → P(nBMA/MMA) → PnBMA (cf. Table 3.1), the collision dynamics are also qualitatively different for all surfaces. Even at higher impact energies, the onset of spreading generally shows similar trends. However, the dimensionless time τ required to reach the maximum extent of spreading becomes progressively higher and the rate of spreading is higher, as expected for higher impact energies. Figure 3.2 demonstrates the qualitative difference between the images presented earlier at a larger velocity U = 1.4119 m/s for the later stages of the impact dynamics. Unlike the lower energy impact shown in Figure 3.1, the recoil/rebound shows appreciable difference even when the solid surface tensions γ_{sv} differ by only 5–6 mJ/m^2 across the polymers (from 39 mJ/m^2 → 35 mJ/m^2 → 29 mJ/m^2).

These behavioral patterns clearly contrasts the scenario for formamide droplet impact on these surfaces. Droplet recoil was so weak that there were no evident distinction in collision dynamics on all 3 surfaces. For the purpose of illustration, the images are shown in Figure 3.3 for the later stages of spread/recoil sequence at the highest impact velocity U = 2.1178 m/s. For all cases considered, the values of β_{max} for water droplet impact are higher than those of formamide droplets. These observations may seem counterintuitive since the impact Weber numbers for formamide is

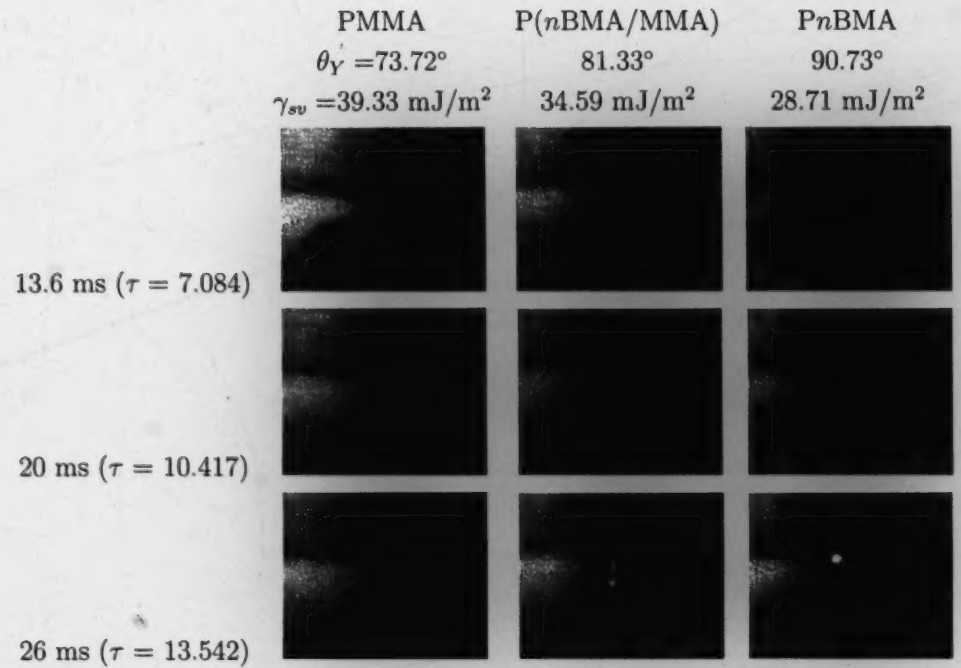

Figure 3.2: Sequential images of a 2.7107 mm water droplet impacting on PMMA, P(nBMA/MMA) and PnBMA surfaces at an impact velocity U = 1.4119 m/s. The differences in the behavior of water droplets were due to incremental variations of the solid-vapor surface tensions γ_{sv}. Contact angles θ_Y and solid-vapor surface tensions were obtained from [16].

larger than that of water for all cases (see Table 3.2). However, since the Reynolds number (*Re* is the ratio of the inertia force to the viscous force) for water droplets is considerably higher than that of formamide droplets (Table 3.2), the difference can then be attributed to the fact that viscous energy dissipation on the water droplets during spread is lower.

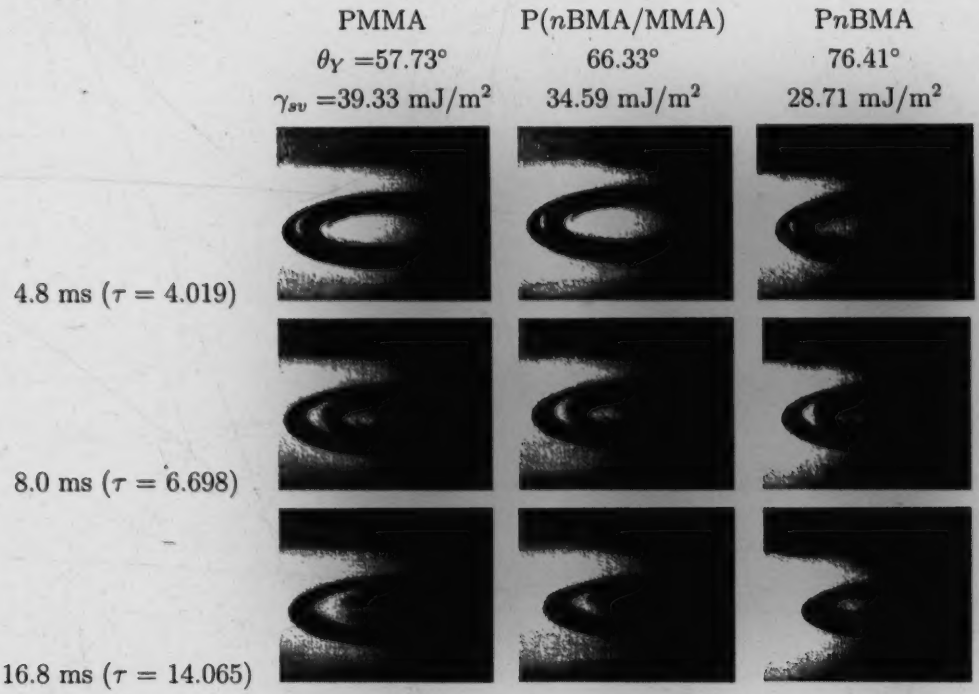

Figure 3.3: Sequential images of a 2.5296 mm formamide droplet on PMMA, P(nBMA-/MMA) and PnBMA surfaces at an impact velocity U = 2.1178 m/s. The differences in the behavior of formamide droplets were due to incremental variations of the solid-vapor surface tensions γ_{sv}. Contact angles θ_Y and solid-vapor surface tensions were obtained from [16].

The summary of the foregoing discussion is that droplet impact dynamics is influenced mainly by the Weber number, Reynolds number and solid-liquid wettability, defined by the contact angle. This has also been verified by a numerical simulation performed by Healy [52], whose results support the relevance of the physical

parameters outlined above on the determination of maximum spreading factor β_{max}. However, question arises as to what extent literature models have captured the essential differences in parametric studies for the determination of β_{max}, irrespective of the impacting liquids and solid surfaces.

3.3.2 Model Predictions and Experimental Data

The search for a model to predict accurately our experimental results forms the basis of this section. As mentioned earlier, there are conflicting reports in the literature concerning the physical parameters that contribute towards the spreading film, and hence, the determination of β_{max}. Based on well-controlled experimental procedures, we have presented data that may readily be used to compare these models in terms of the physical parameters that are most relevant to the determination of β_{max}.

3.3.2.1 Madejski [23]

The model by Madejski [23] implemented a novel analytical method and incorporated viscous dissipation and surface tension effects in their simultaneous solution of fluid kinetics and splat-quenching problem. Madejski considered the spreading film to be cylindrical in shape and expressed the energy lost to viscous dissipation in terms of the shear stresse induced by the velocity gradient in the spreading droplet.

He then employed a numerical analysis which resulted in the degree of flattening of the spreading film as a function of Re, We, Pe (Pe is the Peclet number defined by $Pe = UD_0/a_0$, where a_0 is the thermal diffusivity), and κ, where κ is a dimensionless parameter used by Madejski to represent the degree to which solidificition/freezing arrests the spreading of the drop. When κ is zero, there is no droplets solidifiction. Thus, the final model for the maximum spreading ratio when freezing is precluded (and hence, droplet spread termination is dictated exclusively by surface tension and

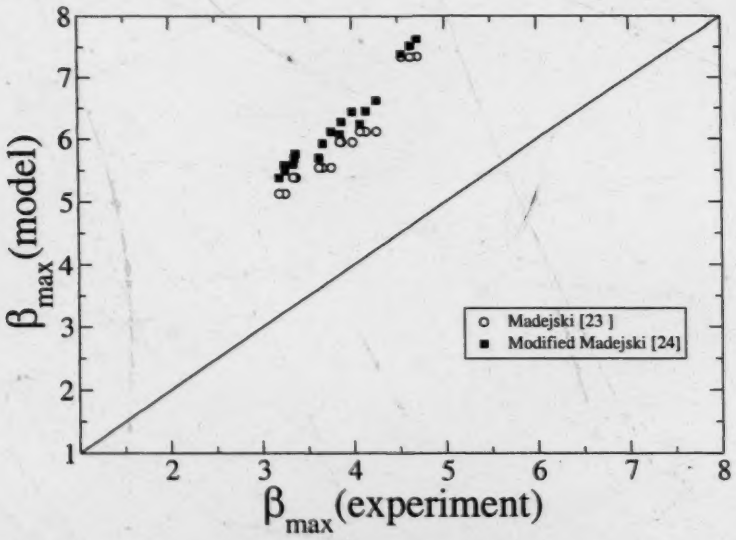

Figure 3.4: Comparison of the model prediction by Madejski [23] and the modified Madejski model by Benneth and Poulikakos [24] with our experimental results. The relative mean error for the Madejski model (circles) is 54.54 ± 5.53% and that for the modified Madejski model (filled squares) is 62.66 ± 5.74%.

viscous energy dissipation) is given as

$$\frac{3\beta_{max}^2}{We} + \frac{1}{Re}\left(\frac{\beta_{max}}{1.2941}\right)^5 = 1. \tag{3.1}$$

Equation (3.1) is valid only for $Re > 100$ and $We > 100$. The limitation on the range of Re and We reduces the number of experimental data that we could use for the validity of Eq.(3.1). The result of the model prediction with our experimental data is given in Figure 3.4. The equation performed badly in modeling the experimental data, yielding a relative mean error of 54.54% with a standard deviation of about 5.53%. One of the most obvious reasons for its failure — besides the neglect of the solid-liquid contact angle — could be the neglect of the surface energy of the droplet before impact. Bennet and Poulikakos [24] also pointed out that the deficiencies of

this model could be improved by incorporating the surface energy terms from the work of Collings et al. [72] and Chandra and Avedisian [11] and including the initial surface energy before drop impact [Eqs. (2), (3), (6), and (17) in Ref. [24]]. The resulting expression is

$$\frac{(\beta_{max}/1.2941)^5}{Re} + \frac{3[(1-\cos\theta_e)\beta_{max}^2 - 4]}{We} = 1. \tag{3.2}$$

where θ_e was defined as the equilibrium contact angle. Unfortunately, the result of this "improved" model prediction was found to yield a relative mean error of 62.66% with a standard deviation of 5.74%, as shown in Figure 3.4 as filled squares. The implication is that even the new model does not account for the energy parameters accurately.

3.3.2.2 Roisman et al [59]

So far, the theoretical model by Roisman et al. [59] appears one of the most rigorous analytical work for drop deformation dynamics. They developed a model for time dependent droplet spreading ratio, $\beta(t)$, by solving the mass and momentum equations of the rim appearing at the edge of the spreading droplet film and within which the liquid is bounded. However, as observed in Chapter 2, their time-dependent model failed to predict the trends of spreading ratios for the tailored surfaces. In addition to $\beta(t)$, they also obtained an approximate expression for the maximum spreading radius which is given below:

$$R_m = \frac{\bar{D}_1}{4} + \frac{\sqrt{6}A\bar{D}_1^2}{8}\sqrt{\frac{1-\cos\langle\theta\rangle}{We}} + \frac{\sqrt{6}}{48A}\sqrt{\frac{We}{1-\cos\langle\theta\rangle}}. \tag{3.3}$$

All the parameters relevant to determine R_m have been defined in Chapter 2.

The model prediction of Eq.(3.3) together with our experimental data are depicted

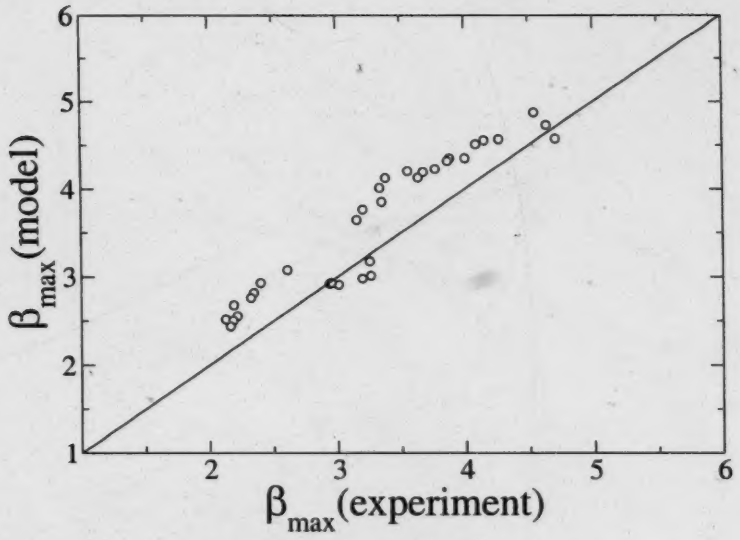

Figure 3.5: Comparison of the model by Roisman et al. [59] with our experimental results. The relative mean error is 12.29 ± 6.69%.

in Figure 3.5. The resulting relative mean error of the model was calculated to be about 12.29% with a standard deviation of 6.69%. Compared to the models of Refs. [23, 24], this appears to be a good model.

3.3.2.3 Modified K-Y model [28]

As Healy et al. [42] compared different model predictions with literature data, they concluded that the Kurabayashi-Yang (K-Y) model [71] provided the most accurate prediction [see Eq.(3.4)]. This informs our choice of the model here for comparison with our experimental data. The K-Y model was originally developed by Kurabayashi and the expression given below is the modified version by Yang [71]:

$$\frac{We}{2} = \frac{3}{2}\left[1 + \frac{3We}{Re}\left(\beta_{max}^2 \ln \beta_{max} - \frac{\beta_{max}^2 - 1}{2}\right) \cdot \left(\frac{\mu_{drop}}{\mu_{wall}}\right)^{0.14}\right] - 6. \qquad (3.4)$$

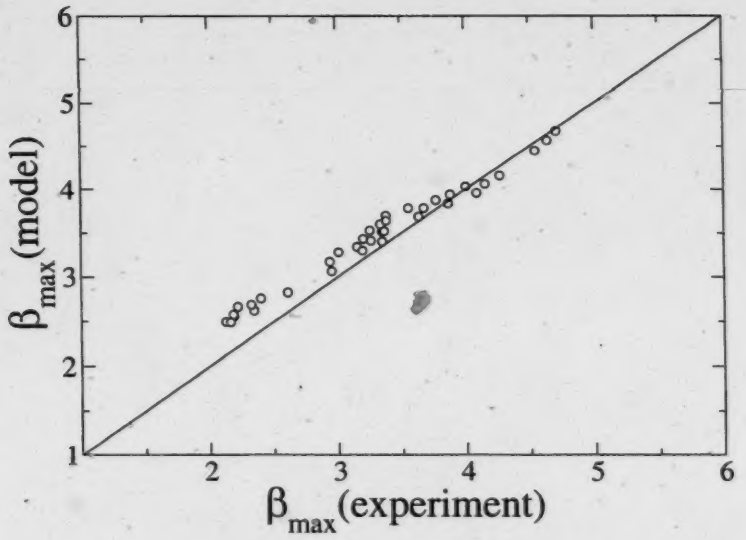

Figure 3.6: Comparison of the modified K-Y model [28] with our experimental results. The relative mean error is 7.10 ± 5.79% .

In subsequent studies [28, 52] using computational fluid dynamics approach, it was observed that the droplet spreading process was highly dependent on the We, Re, and the contact angle θ. The authors therefore concluded that the K-Y model could be improved if wetting effects were incorporated into the model using contact angle. The proposed modification via an empirical fit yielded

$$\beta_{KY,corr} = \beta_{KY} \cdot (45/\theta)^{0.241}. \tag{3.5}$$

Indeed, the modified model prediction showed considerable improvement over the original version. The results are displayed in Figure 3.6. The agreement with our experimental results was good, with a relative error of 7.10 ± 5.79% (mean and standard deviation).

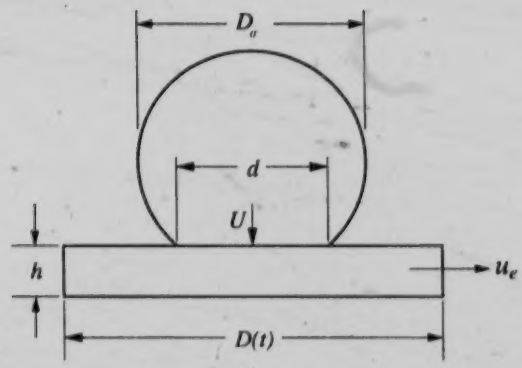

Figure 3.7: Model proposed in Ref. [29] for the spreading droplet. This figure has been exaggerated for clarity: $D(t) \gg h$

3.3.2.4 Pasandideh-Fard et al. [29]

Like most other models, Pasandideh-Fard et al. [29] considered the shape of the droplet at the maximum spread diameter to be cylindrical. The velocity of advance of the contact line was, however, determined by assuming that the droplet, after impact, flows from a spherical cap into the cylindrical base underneath. Figure 3.7 below describes this spreading model vividly. In that figure, u_e is the spreading velocity of the edge of the droplet, and $D(t)$ is the diameter of the droplet at the instant considered. In the model, they assumed that the liquid flows through an area of diameter d with velocity equal to the impact velocity U into the cylindrical base and then outwards. In addition, they also assumed that d varies between 0 and D_0. The model is an improvement on the work presented by Chandra and Avedisian [11].

The authors assumed that the over-prediction of β_{max} in Ref. [11] may be connected to incorrect assumptions associated with the viscous dissipation term. All other terms, namely the initial kinetic energy $[E_{k_i} = (\frac{1}{2}\rho U^2)(\frac{\pi}{6}D_0^3)]$, initial surface energy $[E_{s_i} = \pi D_0^2 \gamma_{lv}]$, and the surface energy $[E_{s_f} = \frac{\pi}{4}D_{max}^2 \gamma_{lv}(1 - \cos\theta_a)]$ at the maximum spread, are similar. Chandra and Avedisian [11] approximated the work

done against viscosity as

$$W \approx \mu \left(\frac{U}{L}\right)^2 \Omega t_c, \tag{3.6}$$

where Ω is the volume of the viscous fluid and t_c is the time taken to reach the maximum spreading extent. By assuming that the characteristic length scale in the y direction was of the order of the splat thickness at the maximum spread, the predicted value of β_{max} was found to be significantly higher than experimentally determined value. A new length scale, equivalent to the boundary layer thickness (δ) at the solid-liquid interface, calculated as $\delta = 2D_0/\sqrt{Re}$ was proposed in Ref. [29] to refine this length scale. In addition, by making assumptions for the droplet shape from the onset of spreading to the maximum spread, t_c, as given in Figure 3.7 was approximated as equal to $(8D_0)/(3U)$ and the volume term as $\Omega = \pi D_{max}^2 \delta/4$. Thus, W is derived as

$$W = \frac{\pi}{3} \rho U^2 D_0 D_{max}^2 \frac{1}{\sqrt{Re}}. \tag{3.7}$$

Combining all the energy terms gives β_{max} as

$$\beta_{max} = \sqrt{\frac{We + 12}{3(1 - \cos\theta_a) + 4(We/\sqrt{Re})}}. \tag{3.8}$$

θ_a was defined as the dynamic advancing contact angle at the maximum spread, and is supposedly measured from the final shape of the droplet at the maximum extent of spread.

Figure 3.8 is a plot of comparison for the model prediction of Eq.(3.8) with the experimental data. The model agreement with the experimental data was excellent with a mean error of 6.57% and a standard deviation of 7.33%.

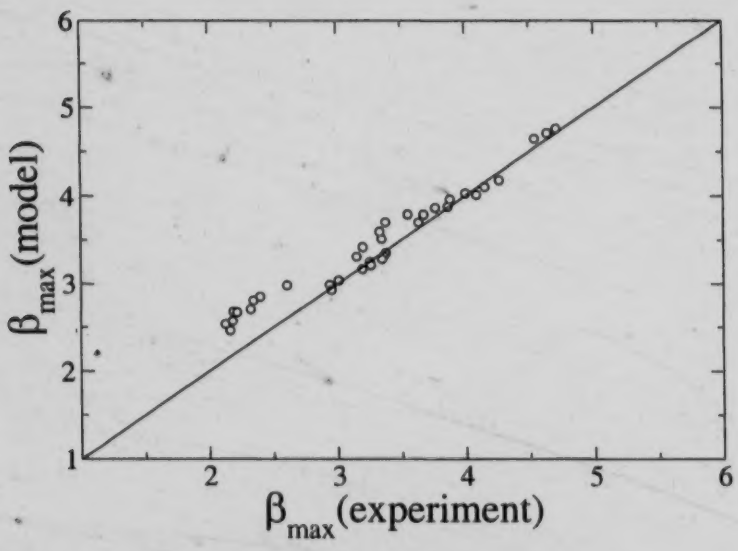

Figure 3.8: Comparison of the Pasandideh-Fard et al. model [29] with our experimental results. The relative mean error is 6.57 ± 7.33%.

3.3.2.5 Refinement of the Models

Clearly, the model prediction by Madejski [23] is far from accurate. Thus, it needs no further consideration or modification(s). However, although the model by Pasandideh-Fard et al. [29] was found to agree well with our data, it is possible to obtain better agreement if we carefully consider the surface energy term at the maximum spread. It is likely that this surface energy term has been under-predicted. To start with, we recall that the cylindrical model was adopted as the assumed shape for the splat at the maximum spread, with a base diameter D_{max} and height h. Though this does not appear to be valid in most cases, especially at higher impact energy and for surfaces with high wettability (low value of equilibrium contact angle), it is apparent that this is still a reasonable approximation for a wide range of practical conditions. The principal difference between the cylinder model and the shape of the actual drop at the maximum extension is the presence of circular ridges and a pronounced rim at

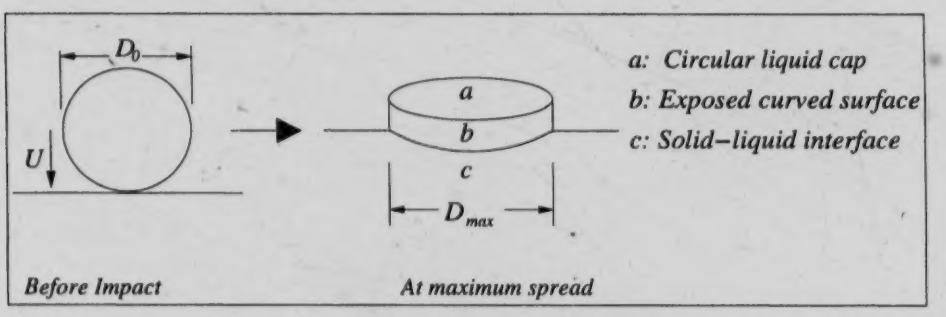

Figure 3.9: An idealized cylindrical model for the maximum spread diameter.

the outer portions of the splat, as observed in the photographs given earlier in Figs. 3.1, 3.2 and 3.3. Figure 3.9 is an explicit representation of the cylinder model often used by most authors.

The cylinder is in contact with three interfaces; thus, the surface energy is the sum of the energy of the droplet in contact with the surrounding vapor $\pi\gamma_{lv}(D_{max}h + D_{max}^2/4)$ and that with the solid surface $\pi D_{max}^2(\gamma_{sl} - \gamma_{sv})/4$ [73]. γ_{sl} and γ_{sv} given in the latter are thermodynamic properties of the system and hence should be constant during the drop impact process. Since they are not readily available for most systems, we may simplify the expression by using the Young Equation (Eq. 1.1) to obtain the surface energy at the maximum spread in terms of θ_Y:

$$E_{s_f} = \pi\gamma_{lv}D_{max}h + \frac{\pi}{4}\gamma_{lv}D_{max}^2(1 - \cos\theta_Y), \tag{3.9}$$

where θ_Y is the Young contact angle. The use of the equilibrium contact angle in the literature associated with this derivation is incorrect. As is well known, there are many metastable contact angles which are also equilibrium angles. Only the advancing contact angles on a smooth (and heterogeneous) surface represent the true surface energetics as given by Young's equation [16].

Several authors [11, 24, 29] have proposed the use of the "advancing" contact angle at the maximum spread to be a more reasonable estimate. Although this may appear more "rational" at first, we note, however, that the origin of the expression for the solid-liquid and solid-vapor interfacial tensions can only be linked to γ_{lv} and θ_Y through the Young equation. This "advancing" contact angle at the maximum spread β_{max} is different from the conventional definition of advancing angle in the determination of solid surface tensions via Young's equation [16]. To avoid confusion, one should have considered such an "advancing angle" as a hydrodynamic angle $\theta_{\beta_{max}}$ at β_{max} which is different from θ_a and θ_Y. While there are also a number of thermodynamic equilibrium contact angles, they are not necessarily equal to θ_Y [16]. In general, the experimentally observed apparent contact angle θ may or may be equal to the Young contact angle θ_Y. For example, on ideal solid surfaces, there is no contact angle hysteresis and the experimentally observed contact angle is equal to θ_Y. On smooth, but chemically heterogeneous solid surfaces, θ is not necessarily equal to the thermodynamic equilibrium angle. Nevertheless, the experimental advancing contact angle θ_a can be a good approximation of θ_Y. This has been illustrated using a model of heterogeneous (smooth) vertical strip surfaces [74]. Therefore, care must be exercised to ensure that the experimental apparent contact angle θ is the advancing contact angle in order to be inserted into Young's equation. On rough solid surfaces, no such equality between advancing contact angle and θ_Y exists. Thus, all contact angles on rough surfaces are meaningless in terms of Young's equation. While the value of $\theta_{\beta_{max}}$ at the maximum spread may be very close to θ_Y in some cases, it is nonetheless incorrect, as $\theta_{\beta_{max}}$ at β_{max} has to involve some degree of hydrodynamics and does not represent exclusively the surface energetic effect given by Eq.(1.1) via θ_Y. Therefore, the use of the equilibrium contact angle in Eq.(3.9), does not arise from the assumption that it is equivalent to the advancing contact angle; but rather,

from a direct substitution of the original Young's equation leading to the surface tensions of the solid-vapor and solid-liquid interfaces with quantities that are more easily measurable — γ_{lv} and θ_Y.

Combining the equations for the different energy terms and using the viscous term of Pasandideh-Fard et al. [29] results in a new expression for the maximum spreading ratio as

$$(We + 12)\beta_{max} = 8 + \beta_{max}^3[3(1 - \cos\theta_Y) + 4\frac{We}{\sqrt{Re}}] \tag{3.10}$$

The principal difference between Eq.(3.10) and that obtained by Pasandideh-Fard et al. [29] is the surface energy term at the maximum spread. Eq.(3.10) was found to give a relative mean error of 4.97% and a standard deviation of 5.05%. For the purpose of comparison, this and similar results for the other models considered are also summarized in Table 3.3. Figure 3.10(a) shows the comparison of results predicted by Eq.(3.10) and our experimental data. In Figure 3.10(b), we have also compared the model prediction with the experimental data used in Ref. [29] (including Refs. [11, 29, 73, 75, 76]). The excellent agreement shown in the two figures is striking. It should be point out that the data in Figure 3.10(b) with the largest deviation are those due to the impact of paraffin wax on aluminum surface where θ_Y is likely to have some degrees of uncertainty. Obviously, accurate examination of such models would require careful experimentation of impact dynamic data on well-prepared and characterized surfaces such as that presented here.

We also observed earlier from the experimental results that the dimensionless time τ to reach β_{max} increases as the impact velocity and drop size increases. However, Pasandideh-Fard et al. had calculated this time to be a constant as 8/3, and independent of the impact velocity. This is likely to be another source of error in the model. The degree of difference in computing β_{max} is not likely to affect the result

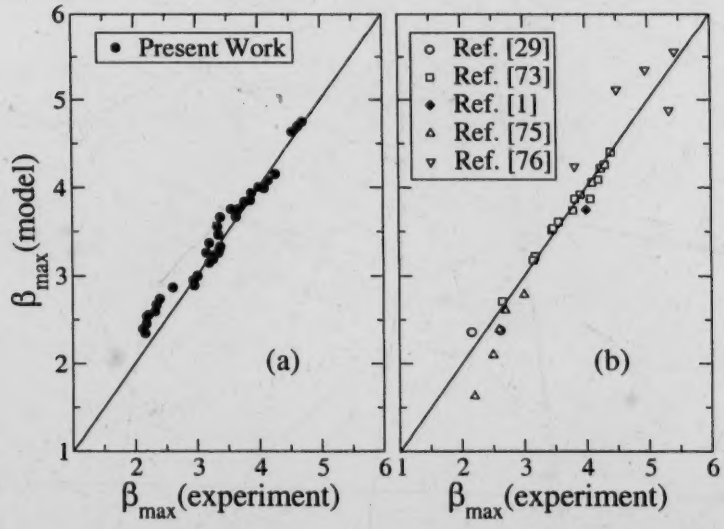

Figure 3.10: Comparison of Eq.(3.10) [our modified model] with (a) our experimental data and (b) results from data used in Ref. [29]. The relative mean error for (a) is 4.97 ± 5.05%.

sharply. Nonetheless, we may seek alternative derivations for the viscous energy term. Benneth and Poulikakos [24] had opined that the treatment of the viscous dissipation term in Ref. [23] was "sound". Based on this premise, we modified the model in Eq.(3.10) by using the extracted viscous dissipation term of Madejski [Eq.(17) in Ref. [24]: $E_v = (\pi/12)\mu D_0^2(\beta_{max}/1.2941)^5]$ to obtain

$$(We + 12)\beta_{max} = \frac{1}{(1.2941)^5} Ca\beta_{max}^6 + 3(1 - \cos\theta_Y)\beta_{max}^3 + 8. \qquad (3.11)$$

Unfortunately, the result of this new model was far from reliable, since it yields a mean error of 58.13 ± 5.91%. Indeed, this result is not very surprising as the modification presented earlier using this viscous energy term in Eq.(3.2) to the Madejski model did not yield any appreciable improvement. This calls to question the use of this equation in deriving the model equation for β_{max} in their work. If they had compared the

Table 3.3: Summary of error analysis of the model predictions for our experimental data.

Model	RME* (%)	SD** (%)	number of data points
Madejski, Eq.(3.1) [23]	54.54	5.53	18
Modified Madejski, Eq.(3.2) [24]	62.66	5.74	18
Roisman et al., Eq.(3.3) [59]	12.29	6.69	33
Modified K-Y, Eq.(3.4) [28]	7.10	5.79	36
Pasandideh-Fard et al., Eq.(3.8) [29]	6.59	7.33	36
Modified Pasandideh-Fard, Eq.(3.10) [this work]	4.97	5.05	36

* Relative mean error
** Standard deviation

prediction with experimental data, they would have seen the deficiency of the model. For now, it is sufficient to assert that the viscous dissipation term by Pasandideh-Fard appears reasonable.

Indeed the need to develop a "perfect" model for predicting the maximum spreading diameter β_{max} remains a subject of vital importance. However, the contention remains the same in all cases: the choice of a viable shape for the spreading liquid droplet and a reasonably accurate model for the energy lost to viscosity as the liquid is deformed during spread. Of course, accurate experimental data on carefully prepared surfaces for testing any such models is a prerequisite.

3.4 Conclusions

We have presented a comparative analysis of literature models for the maximum spreading diameter of liquid droplets on impact with solid surfaces using experimental results from the impact of water droplets (original diameters $D_0 = 2.7107$ and 3.628 mm) and formamide droplets ($D_0 = 2.5296$ mm) on three carefully prepared polymer surfaces: [PMMA, P(nBMA/MMA) and PnBMA] at impact velocities ranging from 0.7059 m/s to 2.7932 m/s. The solid surfaces were prepared with great care to ensure

that the observed fluid dynamic behaviors were due exclusively to surface wettability (excluding roughness). In addition, observation of our experimental results also shows that drop impact dynamics is influenced by impact energy of droplet at impact, physical properties of the liquid droplets, and solid surface tensions. It was found that literature models that neglected these conditions modeled our experimental results with more pronounced errors. Modifying the final surface energy term of Pasandideh-Fard et al. yielded good improvement in the determination of the maximum spreading diameter with a mean error of $4.97 \pm 5.05\%$. However, the complications involved in deriving the maximum spreading diameter remains largely unresolved since other physical parameters such as surface roughness have not been accounted for.

CHAPTER 4

ON WETTABILITY AND THE MAXIMUM SPREADING DIAMETER

4.1 Introduction

The complexities involved in modeling time-dependent spreading ratio $\beta(t)$ on solid surfaces with differential wettabilities has been critically examined in Chapter 2 using two literature models. While Shi and Chen [46] neglected wettability in their final model, Roisman et al. [59] accounted for wettability using the dynamic advancing contact angle. Both models, however, failed to accurately predict the temporal evolution of the spreading film.

The analysis of model prediction studies for droplet dynamics was extended in Chapter 3 to include all relevant energy parameters that was shown to govern the behavior of the droplets during spread on the solid surfaces for the determination of β_{max}. In order to justify the accuracy of the comparative analysis, it was ensured that careful experimental procedure was followed in preparing the target surfaces and also in the image capture techniques of the impinging droplets.

In the models considered in Chapter 3, it was observed that there were variations in the definition of the relevant energy parameters that govern droplet spread. Of all

these parameters, the surface energy is more readily tailorable since it also includes the contact angle as one of the input parameters. To this end, this chapter explores this avenue to offer improved understanding for the collision dynamics of the impacting droplets by way of tailored surface energetics.

The central aim of this chapter, therefore, is to report a systematic study of droplet dynamics on carefully prepared monolayer surfaces that are tailored to yield different wettabilities. Chemically, the monolayers differ only in their relative percentages of mixture between methyl CH_3 and carboxylic acid CO_2H groups. Most of the models employed in Chapter 3 to predict β_{max} will also be compared with those from the experiments given in this Chapter.

Specifically, the surface characterization techniques employed here involve probing the surface for its chemical functionality and determining the wettabilities via contact angle measurements, with a view to link the physics of drop impact dynamics with solid surface properties. Using two parent SAMs of a hydrophobic 1-octadecanethiol [$HS(CH_2)_{17}CH_3$] and a hydrophilic 16-mercaptohexadecanoic acid [$HS(CH_2)_{15}CO_2H$], 5 mM of this binary mixture solution in four different volume fractions was employed for molecular assembly on metal-based surfaces. Analytical tools such as Fourier Transform Infrared Spectroscopy (FT-IR) will be used to determine its chemical functionality. Contact angles measurements by means of an axisymmetric drop shape analysis - profile (ADSA-P) will be employed to characterize wettability. It will be shown that the outcome of such molecular assembly and surface modification leads to extremely different collision dynamics.

4.2 Experimental Procedures

In order to obtain the wide range of wettability mentioned above, SAMs on gold-coated substrates (described in Chapter 2) will be prepared by coadsorption of 1-

octadecanethiol $HS(CH_2)_{17}CH_3$ and 16-mercaptohexadecanoic acid $HS(CH_2)_{15}CO_2H$ in four different volume fractions of CH_3:CO_2H (70:30, 50:50, 30:70, and 10:90). In this chapter, as in Chapter 2, the terms CH_3 and CO_2H will be employed to represent the 1-octadecanethiol and 16-mercaptohexadecanoic acid, respectively.

Supported gold films for the SAMs were prepared using the same method described earlier. For the purpose of contact angle measurements, holes of about 1 mm diameter were made using a diamond drill bit from Lunzer (New York, N.Y.; SMS-0.027), in the center of each wafer surface and cleaned thoroughly using acetone before the thermal evaporation of gold. The substrates were immersed into these solutions for at least 4 hr, and the resulting surfaces were rinsed with ethanol and blow dried by nitrogen before use.

The procedures for characterization of SAMs using the Fourier Transform Infrared (FT-IR) has been described in Chapter 2. For wettability characterization (to determine the contact angles of water on the modified surfaces), a Linux version of the axisymmetric drop shape analysis – profile software (ADSA-P) was used for the sessile drop measurements of water on the mixed SAMs. ADSA-P is a technique to determine liquid-fluid interfacial tension and contact angles from the shape of axisymmetric menisci, i.e., from sessile as well as pendant drops [77, 78]. Assuming that the experimental drop is Laplacian and axisymmetric, ADSA-P finds a theoretical profile that best matches the drop profile extracted from an image of a real drop, from which the surface tension, contact angle, drop volume, surface area and three-phase contact radius can be computed. The strategy employed is to fit the shape of an experimental drop to a theoretical drop profile according to the Laplace equation of capillarity, using surface tension/interfacial tension as an adjustable parameter. The best fit identifies the correct surface tension from which the contact angle can be determined by a numerical integration of the Laplace equation. Details of the ADSA-P technique

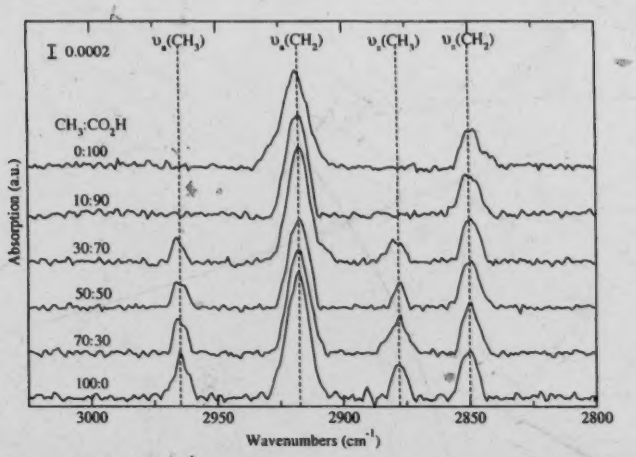

Figure 4.1: Grazing incident polarized infrared spectra for mixed SAMs of 16-mercaptohexadecanoic acid and 1-octadecanethiol in four different ratios. The approximate positions of methylene modes are 2918(asym) cm^{-1} and 2850(sym) cm^{-1}, and those for the methyl modes are 2964(a-sym) cm^{-1}, and 2879(sym) cm^{-1}. The spectra have been offset vertically for clarity.

can be found in Refs. [77, 78].

The cleaning procedures described earlier and the same droplet image capture system have also been used in the experiments whose results are given below.

4.3 Results and Discussion

4.3.1 Surface Characterization using FT-IR and ADSA-P

The reflectance spectra of the four mixed SAMs are given in Figure 4.1. Spectra for the pure 16-mercaptohexadecanoic acid and 1-octadecanethiol monolayers are also included to facilitate better understanding of the results. The plot shows that the asymmetric methylene peaks $\nu_a(CH_2)$ appeared around 2918 cm^{-1} and the symmetric methylene peak $\nu_s(CH_2)$ at 2850 cm^{-1} for all spectra. There is no significant difference between the peak intensities of the symmetric methylene $\nu_s(CH_2)$ except that they

Table 4.1: Advancing contact angle of water θ_a (degree) and solid-liquid work of adhesion W_{sl} (mJ/m^2) for mixed SAMs. The dimensionless time $\tau = tU/D_0$ to reach a maximum spreading ratio and an initial spreading film velocity u_e/U during the first 4.4 ms are also shown.

Volume fraction of mixed SAMs (CH_3:CO_2H)	θ_a	W_{sl}	τ	u_e/U
70:30	113.0	44.4	1.81	1.55
50:50	102.3	57.6	2.17	1.84
30:70	91.0	71.4	2.53	1.86
10:90	55.8	113.6	2.89	2.38

decrease slightly from 30:70 to 0:100. The peak positions of the symmetric as well as the asymmetric (CH_2) stretching vibrations are known to be sensitive indicators of the ordering of the alkyl chains [79]. It is also clear in Figure 4.1 that the widths and positions of the peaks remain relatively unchanged, indicating that these SAMs' structures are crystalline. In terms of the asymmetric and symmetric methyl peaks, they appear at 2879 and 2964 cm^{-1}, respectively. A decreasing trend is apparent as the CH_3 fraction (methyl end group) decreases. The relative amount of these peaks indicate how much the IR "sees" in terms of the exposed terminal CH_3 group. Thus, mixed SAMs with the lowest percentage of CH_3 (10:90) shows nearly no methyl peaks, even when a 10% volume fraction of CH_3 was selected. These results indicate that the surface composition/concentration of mixed SAMs can be slightly different from what one would expect by mixing the same amount of volume fraction in the solution for molecular assembly.

In terms of the advancing contact angles of water, Table 4.1 summarizes the results for different CH_3:CO_2H volume fractions of 70:30, 50:50, 30:70, and 10:90. The results reflect the nature of the adsorbed SAMs as described in the FT-IR results given above and also confirm the sensitivity of water contact angle to the exposed terminal groups. The mean advancing contact angles varies from $\theta_a = 113.0°$ (for the

most hydrophobic 70:30 mixed SAMs) to $\theta_a = 55.8°$ (for the most hydrophilic 10:90 mixture). The contact angle results in Table 4.1 represent an average of at least 3 and up to 5 independent measurements. We see that the advancing contact angles are extremely sensitive to minute variation of chemical components on the surface. Hence, careful experimentation is required for solid surface preparation in order to explore the underlying physics of droplet impact dynamics.

4.3.2 Droplet Impact Scenario

Figure 4.2 shows a sequence of images for the impact of water droplets onto four mixed SAMs in the CH_3:CO_2H ratios of 70:30, 50:50, 30:70 and 10:90 for $We = 60$ and $U = 1.0936$ m/s. The drop impact dynamics for all surfaces can be summarized into several phases: (1) initial spreading at a velocity generally higher than the impact velocity; (2) deceleration of the spreading film towards the maximum spreading diameter; and (3) a weak re-spreading characterized by mild oscillations towards equilibrium configuration. The observed differences in collision dynamics reflect only the differential wettabilities of the mixed SAMs with water.

Going from the mixed SAMs with a 70:30 to 10:90 ratios, there is an observable increase in the area wetted by the water droplets. In all cases, the droplet spreads out radially and finally assumes a very thin disc-like shape. The time taken to reach this configuration varies from one to another surfaces. In particular, for the more hydrophilic surfaces (10:90), it takes a longer time for the drop to reach the maximum spreading diameter β_{max}. A summary of the dimensionless time τ to reach β_{max} and a normalized spreading velocity u_e/U during the first 4.4 ms for all surfaces is also shown in Table 4.1. However, it was observed that, as the hydrophobic 70:30 and 50:50 SAMs have reached their β_{max}, the spreading diameters β for the other surfaces (30:70 and 10:90) are still increasing. This implies that the spreading rate for droplets

on the more hydrophilic surfaces (the latter two) are generally higher.

In Figure 4.2, the images also indicate that there is a wave (or circular rings) that travels towards the edge of the droplet as they approach the maximum diameter β_{max}. For the case of the 10:90 SAMs, this wave travels back and forth along the surface area of the splat after it has reached the maximum diameter; nevertheless, the change from the maximum diameter appears to be insignificant. Typically, a thin film at the periphery of the splat remains attached to the solid surface while circular rings in the inner region move back and forth as an attempted retraction sequence. The resistance to this recoil motion is due to a strong droplet/surface interaction and results in a wavy motion within the droplet. On the contrary, the waves travel back with a high velocity during the recoil motion for the other fractions and become dissipated as the droplet rebounds axially.

Since the rebound motion also depicts the surface energy characteristics of the surface, it is interesting to observe the phenomenon more closely. Typically, our results show that the rebound height increases as contact angle (or surface hydrophobicity) increases. Obviously, this results from the repulsive intermolecular forces between water molecules and functional groups that are exposed to the mixed SAMs surfaces. Hence, after reaching the maximum diameter, the liquid film retracts from the wetted portion of the surface and undergoes rapid rebound and oscillations in attempt to reduce their exposure to the solid surface. This behavior is directly related to the work of adhesion W_{sl} between water and the surfaces; that is, there is more rebound when W_{sl} decreases. Figure 4.3 shows typical images of droplet rebound on the four surfaces at time $t = 32$ ms after initial contact with the solid surfaces. Although the droplet did not split into several tiny droplets during the rebound even for the most pronounced case (fraction 70:30), we note that, during the axial (vertical) stretching of the droplets, a tiny droplet with a diameter about one-third the original droplet

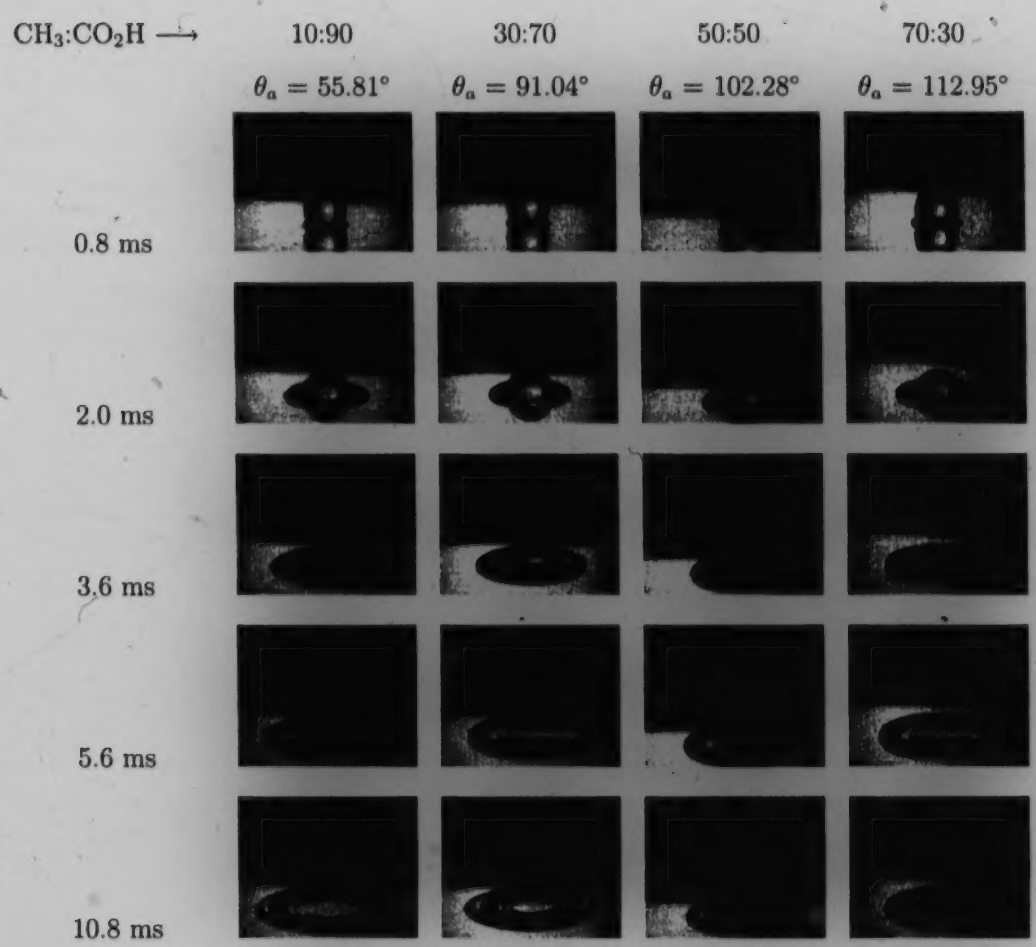

Figure 4.2: Impact of water droplets on mixed SAMs of 1-octadecanethiol and 16-mercaptohexadecanoic acid in CH_3:CO_2H volume fractions of 10:90, 30:70, 50:50 and 70:30. θ_a is the advancing contact angle of water (continued on next page)

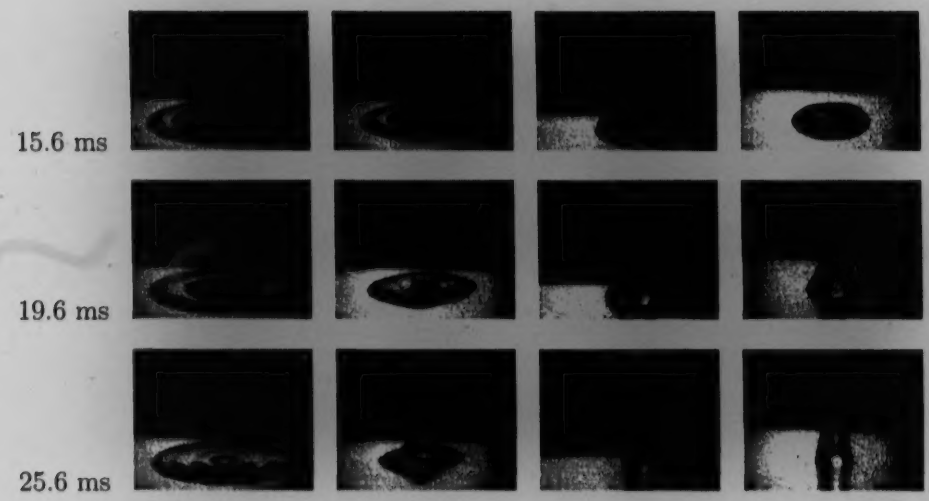

Figure 4.2: Impact of water droplets on mixed SAMs of 1-octadecanethiol and 16-mercaptohexadecanoic acid in CH_3:CO_2H volume fractions of 10:90, 30:70, 50:50 and 70:30. θ_a is the advancing contact angle of water.

diameter separated from the parent droplet. The extent of the droplet axial motion may be explained in terms of the surface energy accumulated during the spreading. The larger the value of θ_Y, as in the case of the 70:30 mixture as given Table 4.1, the higher the surface energy accumulated as the droplets approach the maximum spreading diameter. This accumulated energy then acts as the springboard for the recoil process.

Thermodynamically, the work of adhesion W_{sl}, also known as the free energy of adhesion, is equal to the work required to separate a unit area of the solid-liquid interface:

$$W_{sl} = \gamma_{lv} + \gamma_{sv} - \gamma_{sl} \tag{4.1}$$

This may also be expressed as

$$W_{sl} = \gamma_{lv}(1 + \cos\theta_Y) \tag{4.2}$$

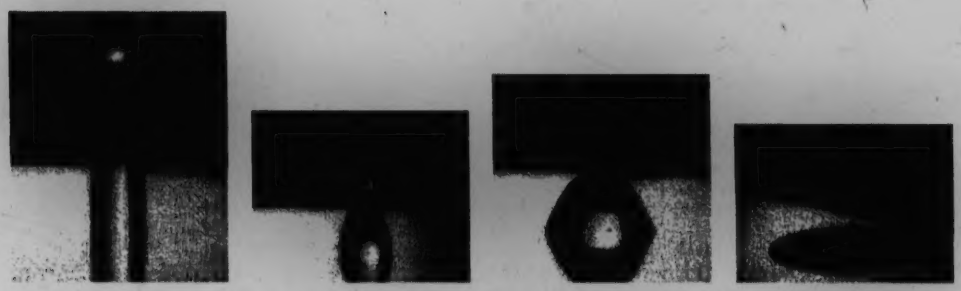

(a) (70:30);	(b) (50:50);	(c) (30:70);	(d) (10:90);
$W_{sl} = 44.4$	$W_{sl} = 57.6$	$W_{sl} = 71.4$	$W_{sl} = 113.6$

Figure 4.3: Axial rebound for mixed SAMs of 1-octadecanethiol and 16-mercaptohexade-canoic acid at $t = 32$ ms after impact. The fractions represent relative volume percentages of CH_3:CO_2H and W_{sl} is the thermodynamic solid-liquid work of adhesion in mJ/m^2.

assuming that Young's equation (Eq. 1.1) holds true. If we also assume that the advancing contact angles θ_a equal θ_Y, an estimate of the work of adhesion for all surfaces can be obtained and are given in Table 4.1. It is obvious that W_{sl} increases as the contact angle decreases, for the surfaces. Such differences in the W_{sl} values directly affect the impact dynamics of water droplets on the mixed SAMs in Figure 4.3.

The general observation for the initial phase of spreading is that inertia effects predominate at these stages. However, as droplet advances, surface energy effect becomes considerably more important than that of inertia. Thus, the restraining effect is stronger on the more hydrophobic surfaces. When water droplet impinges on the surface with a high impact energy, it deforms and stretches appreciably. For the case of hydrophobic surfaces, this exposure is not thermodynamically favorable for the solid-liquid interface. Hence, the droplet recoils with a velocity that commensurates with the impact energy and the extent of deformation, causing axial rebound.

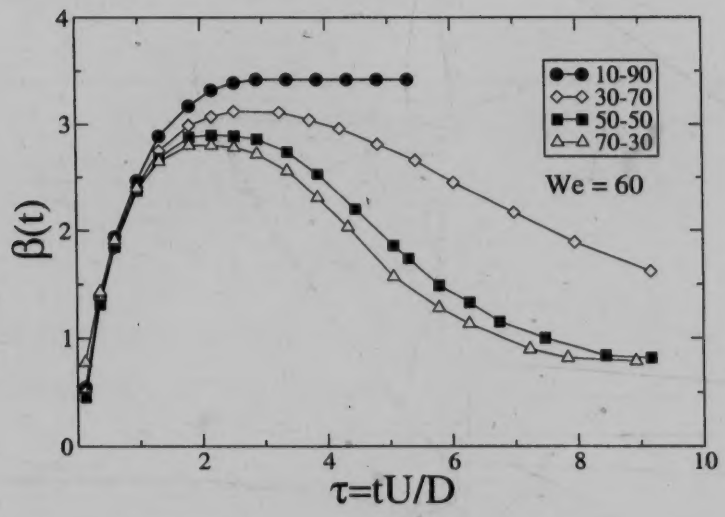

Figure 4.4: Time evolution of droplet spreading diameter $\beta(t)$ on mixed SAMs with CH_3:CO_2H volume fractions of 10:90, 30:70, 50:50, and 70:30.

Figure 4.4 shows the time evolution of the area wetted by the impacting water droplet using spreading factor ($\beta(t) = D(t)/D_0$) as a parameter. The result shows that, within the early times in the range $0 < \tau < 1.3$, the spreading factors are approximately equivalent for all surfaces. The spreading pattern changes, however, as time progresses: within the dimensionless time between $1.3 < \tau < 2.1$, the difference in the spreading rates becomes more obvious. Moreover, the recoil sequence also illustrates the energetic difference of the mixed SAMs. The maximum spreading factors β_{max} attained by the spreading film is summarized in Figure 4.5 in a plot of β_{max} against the fraction of the 16-mercaptohexadecanoic acid CO_2H in the mixture. For completeness and comparison purposes, we have also included the results for pure SAMs of 1-octadecanethiol (100:0) and 16-mercaptohexadecanoic acid (0:100). We see that, as the CO_2H component in the solution mixture increases, the maximum spread β_{max} increases. This is in agreement with the FT-IR and contact angle results given earlier.

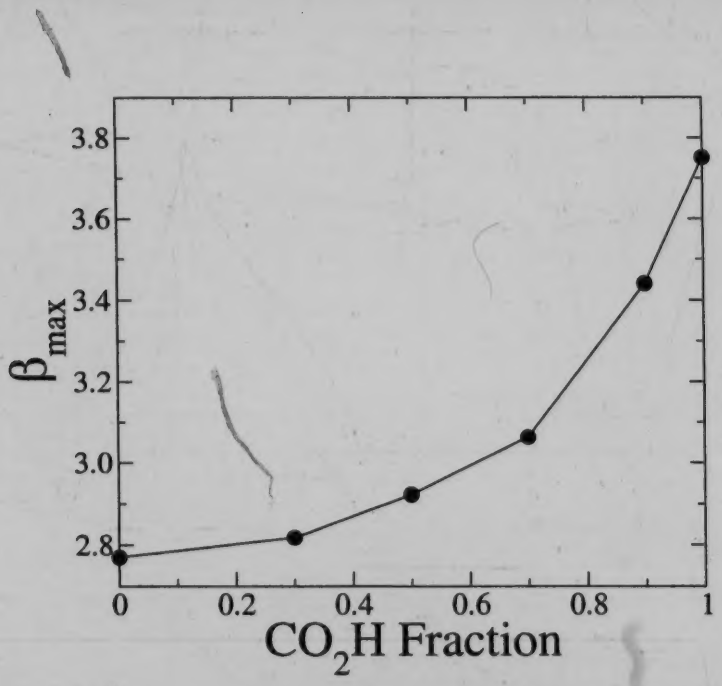

Figure 4.5: Maximum spreading factor β_{max} for mixed SAMs as a function of the percentage of 16-mercaptohexadecanoic acid monolayers CO_2H.

4.3.3 Estimating the Maximum Spreading Diameter

In this section, we seek to explore models that can accurately predict the wetting behavior of water droplet on our tailored surfaces in terms of the maximum spreading ratio β_{max}. It must also be reiterated based on the foregoing discussion that wettability cannot be assumed negligible for most practical situations. In the literature there are several semi-empirical correlations aimed at predicting β_{max}. Apart from wettability considerations, there are other conflicting issues with respect to the appropriate modeling of the energy parameters that contribute towards the spreading droplet as it attains the maximum diameter. We shall show this by the following five model predictions; two of which do not account for wettability. Most of these models have been considered in the previous chapter for the prediction of β_{max} on polymer surfaces and will not be rendered in detail here.

The experimental study by Manzello et al. reported that the semi-empirical model by Shi and Chen [46] (Eq. 2.9) provided a reasonable prediction of their experimental data for predicting $\beta(t)$, and attributed the success to the fact that the model incorporates liquid fluid properties. One of the most pronounced error with the model, however, is the exclusion of wettability. Obviously, it is questionable that this model can account for time variation of droplet spread for our tailored surfaces. The model will also be employed here to predict β_{max} in comparison with the other models with respect to our experimental results.

The other models which will also be employed include: (1) the K-Y model, Eq. (3.4) [71] (does not account for accountability); (2) the modified Kurabayashi-Yang, Eqs. (3.5) (K-Y) model [28, 52] (includes contact angle); (3) the Roisman et al. model, Eq. (3.3) [59] (does not contact angle); (4) the model by Pasandideh et al., Eq. (3.8) [11]; and, (5) the modified version of the model in Ref. [11], given in Eq. (3.10).

The prediction results of the models considered above [including Eq.(3.10)] together with our experimental data are summarized in Table 4.2. The error in predicting the experimental result for each model is given in terms of the mean error and standard deviation. It is clear that the first two models perform badly: The model by Shi and Chen [Eq.(2.9)] under-predicts all the data and the modified K-Y model [Eq.(3.4)] over-predicts them. The remaining models predict the spreading behavior with different degrees of error. Obviously, accurate examination of such models would require careful experimentation of impact dynamic data on well-prepared and characterized surfaces such as those presented here.

Based on error analysis, it is clear that Eq.(3.10) derived in this thesis predicts our experimental results most accurately. We may also examine further the physics of the model by assuming a hypothetical droplets with given physical properties and hence

Table 4.2: Summary of error analysis for the prediction of maximum spreading factor β_{max} from different models.

Solid Surface**	β_{max} (expt)	$\beta_{max,predicted}$					
		Eq.(2.9) [46]	Eq.(3.4) [71]	Eq.(3.5) [28]	Eq.(3.3) [59]	Eq.(3.8) [29]	Eq.(3.10) [this work]
70:30	2.818	2.577	3.862	3.094	3.153	2.997	2.939
50:50	2.922	2.577	3.862	3.169	3.307	3.102	3.044
30:70	3.063	2.577	3.862	3.259	3.475	3.232	3.174
10:90	3.440	2.577	3.862	3.667	3.939	3.740	3.683
RME*(%)		15.32 ± 7.16%	26.89 ± 10.73	7.81 ± 1.61	14.75 ± 1.77	6.69 ± 1.40	4.79 ± 1.54

* Relative mean error
**Solid surface refers to Mixed SAMs fractions (CH_3:CO_2H)

different Reynolds number. In Figure 4.6(a), we set the Weber number We to be 60. The hypothetical solid surfaces are assumed such that θ_Y on these surfaces varies from 15° to 180°. The curves show that, for a given contact angle, β_{max} increases as Re increases. This is to be expected as increasing Re corresponds to a decrease in viscous drag on the spreading film. As can be seen, this variation tends to diminish as contact angle increases. The influence of wettability becomes less significant as Re increases. The model is therefore physically realistic. Similar curves were constructed for We = 150, 500 and 1000 in Figures 4.6(b), (c) and (d), respectively. It can be seen that wetting (contact angle) effect on the maximum spread β_{max} reduces as Weber number increases for the same range of Reynolds numbers. This family of curves could be handy when one considers liquids for use in spray cooling applications as their wetting capacity depends on the maximum spreading diameter β_{max}. Another observation from the curves is that when $15° < \theta < 50°$, maximum spread is influenced more by wetting than by Weber number for a fixed Reynolds number. This is shown in Figure 4.7 by plotting β_{max} with θ_Y for various numbers of We with $Re = 1000$. Thus, for the same Reynold number, maximum spread β_{max} increases as Weber number decreases

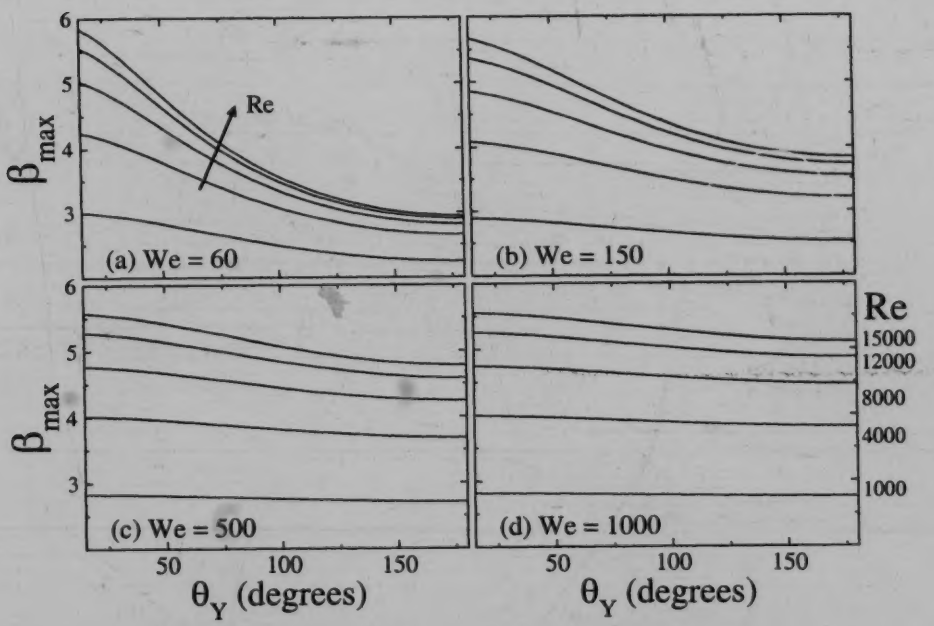

Figure 4.6: Hypothetical situation depicting the influence of wettability, defined by the Young contact angle θ_Y, on the maximum spreading diameter β_{max}. Eq.(3.10) was used to generate the curves for (a) $We = 60$, (b) $We = 150$, (c) $We = 500$ and (d) $We = 1000$, for different Reynolds numbers, $1000 \leq Re \leq 15{,}000$.

between $15° < \theta < 50°$.

4.4 Conclusions

We have carefully engineered solid surfaces with tailored surface energetics and studied the effect of the differential surface energy on the collision dynamics of 3.628 mm diameter water droplets. The solid surfaces were tailored by mixing self-assembled monolayers (SAMs) of 1-octadecanethiol [$HS(CH_2)_{17}CH_3$] and 16-mercaptohexadecanoic acid [$HS(CH_2)_{15}CO_2H$] in the solution mixtures in CH_3:CO_2H ratios of 10:90, 30:70, 50:50 and 70:30. The surfaces generated were examined by means a Fourier Transform-Infrared Spectroscopy (FT-IR), and axisymmetric drop shape analysis – profile (ADSA-

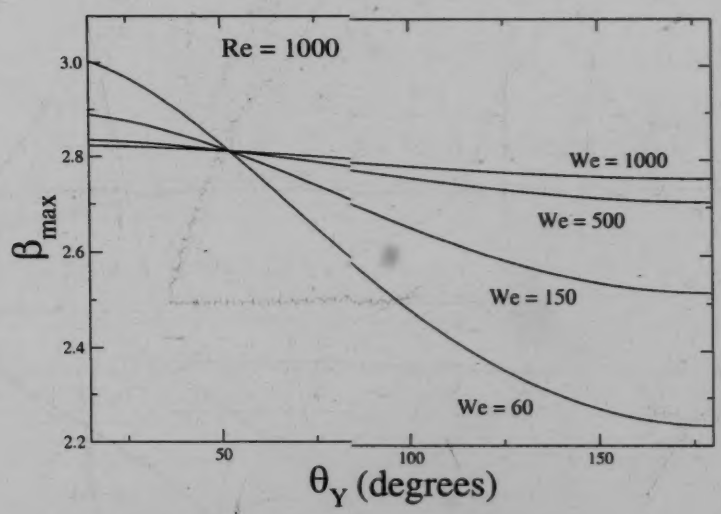

Figure 4.7: Hypothetical situation depicting the influence of wettability, defined by the Young contact angle θ_Y, on the maximum spreading diameter β_{max} for $Re = 1000$ and $We = 60$, 150, 500 and 1000 according to Eq.(3.10).

P) technique for its chemical functionality and contact angle, respectively. Contact angle results indicate that increasing the proportion of the 16-mercaptohexadecanoic SAMs reduces the mean contact angles. This is also supported by the FT-IR spectra which indicate that the intensities of the methyl peaks decreases as the fraction of 16-mercaptohexadecanoic SAMs increases. These differences are reflected on the collision dynamics and is due exclusively to surface energetic variations. Understanding the behavior of impacting droplets in terms of surface energetics has been enhanced by these tailored surface properties in terms of chemical functionality and and wettability. The results for the maximum spreading ratio show that a model that must accurately predict the behavior of impacting droplet on any given surface cannot overlook wettability. In particular, it has also been observed that properly accounting for other sensitive physical parameters, such as the surface energy, predicts the maximum spread more accurately. Obviously, accurate examination of such mod-

els requires careful experimentation of impact dynamic data on well-prepared and characterized surfaces.

Chapter 5

Conclusions and Recommendations

5.1 Conclusions

The collision dynamics of liquid droplets impinging normally on smooth, rigid surfaces have been studied both experimentally and theoretically. Several surface imaging and analytical tools have been used to probe the solid surfaces prior to impact in order to correlate the fluid dynamics of the impacting droplets with solid surface characteristics. Throughout this thesis, it is shown that careful solid surface preparation was essential to obtaining accurate and reliable experimental data for these correlations. Obviously, the contention in the literature as to the factors responsible for terminating the spread of a liquid droplet after impact was shown to be largely due to the absence of reliable experimental data of liquid drop impact on well-prepared and well-characterized solid surfaces to ascertain the validity of these assumptions.

In this work, solid surfaces have been carefully engineered with tailored surface energetics, and the physical phenomena observed during the droplet deformation were correlated with the surface properties of the characterized surfaces. In particular, it was shown that the behavior of impacting droplets on solid surfaces can be altered by even a small variation of chemical functionality ($\sim$ 2 Åin one of the cases considered here) at the solid-liquid interface. Tailored surfaces have been generated using self-assembled monolayers (SAMs) of hydrophobic 1-octadecanethiol and hydrophilic 16-

mercaptohaxadecanoic acid. The resulting surfaces have widely different chemical functionalities that are highly instrumental to the study of systems (e.g. droplet impact) where interfacial phenomena play a predominant role.

The results obtained here corroborate several literature results that support the functional dependence of the form $\beta_{max} = f(We, Re, \theta)$ for the maximum spreading ratio. The exact form of this function based on energy conservation considerations has already been proposed by several authors. Yet, no general consensus exists as to the form of the viscous energy dissipation. As for the surface energy at the maximum spread, it was shown that it is often underpredicted. This explains why the maximum spread diameter is often overpredicted by several models.

The issue of whether wettability influences the spreading behavior of impacting droplets has been laid to rest, since even minor variations in the advancing contact angles resulted in completely different fluid dynamical behavior, as shown in Chapter 4. In addition, β_{max} and the rebound velocity was also shown to be highly sensitive to slight changes in the work of adhesion via contact angles.

5.2 Recommendations

1. Of particular concern is the issue of predicting the maximum spreading diameter more accurately so that industrial processes that rely on the wetting effects of impacting droplets can be significantly improved. Further modifications to the current model for the viscous energy dissipation term at the droplet maximum spread is therefore necessary. There are two parts to this improvement: first, the velocity gradient that induces shear stress at the solid-liquid boundary layer requires refinement. Rather than the order of magnitude approach proposed so far, it is believed that a more elaborate definition could significantly improve the prediction of β_{max}. Second, it may also be appropriate to seek a model of

the type $t_c = F(U, D_0, \rho, \theta)$, where F is a yet-to-be determined function, and t_c is the time for the spreading film to reach the maximum spreading diameter. It will be recalled that t_c was defined in Ref. [29] as constant (= 8/3), whereas the experimental results in this work showed the term to be dependent on U, D_0, ρ, and θ. Once determined, the velocity gradient and the time to reach maximum spread may then be used to redefine the viscous energy term:

$$W = \int_0^{t_c} \int_\Omega \phi dV dt, \tag{5.1}$$

where Ω has been defined earlier as the volume of the viscous fluid, and ϕ is the dissipation function given by

$$\phi = \mu\Big(\frac{\partial v_i}{\partial x_j} + \frac{\partial v_j}{\partial x_i}\Big)\frac{\partial v_i}{\partial x_j} \approx \mu\Big(\frac{du}{dy}\Big)^2. \tag{5.2}$$

2. Several correlations exist to relate liquid and solid surface properties with droplet splashing. However, this study was restricted to conditions where splashing did not occur on impact, i.e. impact energy was "low enough" to avoid splashing. The study could be extended to examine the conditions that result in splashing and to attempt its prediction. Splashing is generally characterized by splitting of the parent droplet into secondary droplets after collision with the solid surface. It is normally enhanced by higher impact velocity and solid surface roughness. Surface roughness induces splashing by the excitation of instability in the spreading film [7]. This instability results in the so-called Raleigh-Taylor (RT) instability, which results when an interface between two liquids is accelerated towards the denser one [39]. The wavelength of the interfacial waves, assuming that the magnitude of the acceleration to be a ($\sim U^2/D_0$

[9]) is given by [80]

$$\lambda = 2\pi\sqrt{\frac{3\gamma_{lv}}{a\rho}}. \tag{5.3}$$

The number of waves around the periphery of the spreading film (these waves result in the formation of fingering patterns that precede the onset of splashing) are then given as [9]

$$N = \frac{\pi D_{max}}{\lambda} = \beta_{max}\sqrt{\frac{We}{12}}. \tag{5.4}$$

Aziz et al [9] proposed that the number of fingers formed around the droplet can be given by

$$N = \sqrt{\frac{We\sqrt{Re}}{48}}, \tag{5.5}$$

if, assuming that splashing occurs only at very high impact velocities, $We/\sqrt{Re} \gg 1$ and $We \gg 12$.

This and other correlations can be tested using experimental data from well-prepared surfaces. In addition, it should be mentioned that the conditions specified above and the substitution for β_{max} were derived from the Pasandideh-Fard model [29] for the maximum spreading ratio which, according to our work here, was shown to be less accurate than the modified version. Rather than adopting the limiting conditions given for the derivation of Eq. (5.5), an attempt might be made to determine N using Eq. (3.10) directly in Eq. (5.4). It is anticipated that this would yield better prediction of N.

3. Since most cases of droplet splashing involve impact of droplet falling from great heights, it may be necessary to incorporate bouyancy and drag on the forces affecting the falling droplets. It should be recalled that the dimensionless numbers derived in this work were functions of the impact velocity, which were determined by simply assuming that the equation of motion holds [i.e., $U =$

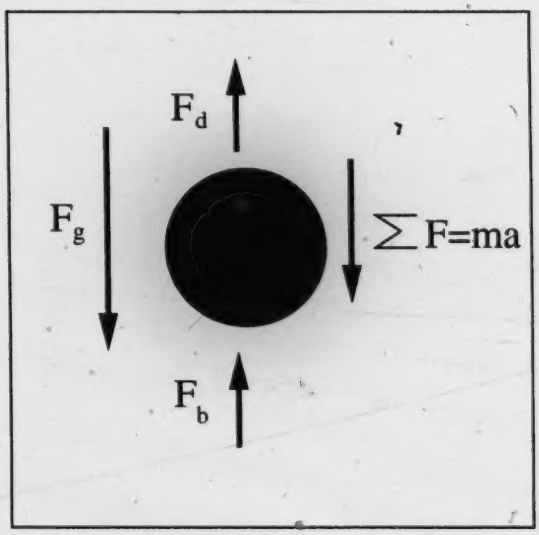

Figure 5.1: Effect of drag and buoyancy on the falling droplet

$\sqrt{2gh}$]. In doing this, it is also assumed that drag and buoyancy do not have any significant effect on the droplet during its flight onto the solid surface. These assumptions could be misleading in certain cases, especially when the droplet is large and impact height is substantial. In that case, friction between a moving drop and the surrounding fluid can result in internal circulation within the drop which accounts for the well-known drag-reduction [81]. In general, this type of internal circulation is normally not considered for drop impact studies [39]. However, we shall determine the extent of the influence of drag and buoyancy on droplets moving through air in order to verify the influence of drag and buoyancy with height of droplet release and offer reasonable recommendation for inclusion of these effects for the computation of U.

Figure 5.1 is a typical drop falling through air with the attendant forces that account for its motion. Assuming that terminal velocity has not been reached (i.e the droplet is still accelerating with a as the acceleration), these forces are

Table 5.1: Impact velocities and other dimensionless parameters for water (D_0 = 3.6280 mm). U_n is determined from Eq. (5.7) while We_n is calculated using U_n

Impact height	velocity (m/s)		Weber number	
(m)	U	U_n	We	We_n
0.0254	0.7059	0.7015	24.8495	24.5400
0.0381	0.8646	0.8582	37.2743	36.7263
0.0610	1.0936	1.0838	59.6388	58.5696
0.4763	3.0570	2.9873	465.9906	444.9726

summed to give the net force

$$\Sigma F = F_g + F_b + F_d = ma = m\frac{dU}{dt}, \tag{5.6}$$

where F_g, F_b and F_d, as given in Eq. (5.6) and in Fig. 5.1 refer to the gravitational, buoyancy and drag force respectively. They are given by $F_g = mg$; $F_b = m\rho_a/\rho g$ (ρ_a is the density of air); and, $F_d = bU$, where b, a form of drag coefficient, is defined as $b = 6\pi\mu D_0/2$. m is the mass of the droplet. Together, these terms result in a differential equation for new impact velocity given by U_n which is then solved to yield:

$$U_n = \frac{mg}{b}(1 - \frac{\rho_a}{\rho})(1 - e^{-bt/m}) \tag{5.7}$$

Using Eq. (5.7) and $U = \sqrt{2gh}$ for the velocities considered in this work for water droplet (D_0 = 3.628 mm), Table 5.1 gives the values of velocities calculated from the two approaches and the attendant Weber numbers. The Reynolds number is a function of U, so it changes only as U changes; hence, its exclusion form the table. As can be seen, the effect of drag and buoyancy becomes more important as the height from which the droplet was released increases. It is particularly more important for the Weber number since it depends on U^2. For the values in Table 5.1, the percentage differences for the

velocity and Reynolds number vary from 0.62% to 2.28%, and for the Weber number, 1.25% to 4.51%. Thus, as the droplet release height increases, the effect of friction and buoyancy forces increases. It may therefore be worthwhile to consider them in such cases when computing U.

4. All the impact examples considered here were for normal impacts only. Also of interest are studies of impact on oblique surfaces, on edges, and on hollow cross-sections. These also find applications in several practical situations.

The present work has studied the behavior of liquid droplets impinging normally on rigid, well-prepared solid surfaces which were well-characterized for various physical and chemical properties before impact. Several literature models were examined and an improvement suggested which was shown to yield a more accurate prediction of the maximum spreading data. An improvement on the model given in the present study could lead to more accurate predictions of the drop impact dynamics.

BIBLIOGRAPHY

[1] W. M. Grissom and F. A. Wierum. Liquid spray cooling of a heated surface. *Int. J. Heat Mass Transfer*, 24:261, 1981.

[2] S. Deb and S.-C. Yao. Anlysis on film boiling heat transfer of impacting sprays. *Int. J. Heat Mass Transfer*, 32:2099, 1989.

[3] M. Ghodbane and J. P. Holman. Experimental study of spray cooling with Freon-113. *Int. J. Heat Mass Transfer*, 34:1163, 1991.

[4] D. Apelian. Perspective on process control in P/M. *Int. J. Powder Metall.*, 28:117, 1992.

[5] E. Gutierrez-Miravete, E. J. Lavernia, G. M. Trapaga, J. Szekely, and N. J. Grant. A mathematical model of the spray deposition process. *Metall. Trans. A*, 20:71, 1989.

[6] F.H. Froes, C. Surayanarayana, E. Lavernia, and G.E. Bobeck. Innovations in light metals synthesis for the 1990s. *SAMPE Q.*, 22:11, 1991.

[7] C. D. Stow and M. G. Hadfiend. An experimental investigation of fluid flow resulting from impact of a water drop with an unyielding dry surface. *Proc. R. Soc. London*, 373:419, 1981.

[8] Kai Range and Francois Feuillibois. Influence of surface roughness on liquid drop impact. *J. Colloid Interface Sci.*, 203:16–30, 1998.

[9] S. D. Aziz and S. Chandra. Impact, recoil and splashing of molten metal droplets. *Int. J. Heat Mass Transfer*, 43:2841–2857, 2000.

[10] L. Bolle and J. C. Moureau. Spray cooling of hot surfaces. In *Multiphase Science and Technology (ed. J. D. Hewitt and N. Zuber)*, pages 1–92. Hemisphere, New York, 1981.

[11] S. Chandra and C. T. Avedisian. On the collision of a droplet with a solid surface. *Proc. Roy. Soc. Lond. A*, 432:13, 1991.

[12] M. Pasandideh-Fard, S. D. Aziz, S. Chandra, and J. Mostaghimi, editors. *Surface cooling by an impinging water drop*, 33rd National Heat Transfer Conference, Albuquerque, New Mexico, August 1999.

[13] M. Pasandideh-Fard, S. Chandra, and J. Mostaghimi. A three-dimensional model of droplet impact and solidification. *Int. J. Heat Mass Transfer*, 45:2229–2242, 2002.

[14] M. Pasandideh-Fard, S. D. Aziz, S. Chandra, and J. Mostaghimi. Cooling effectiveness of a water drop impinging on a hot surface. *Int. J. Heat Fluid Flow*, 22:201–210, 2001.

[15] G. Trapaga, E. F. Matthys, J. J. Valencia, and J. Szekely. Fluid flow, heat transfer and solidification of molten metal droplets impinging on substrates : comparison of numerical and experimental results. *Metallurgical Trans. B*, 23B:701–718, 1992.

[16] D. Y. Kwok and A. W. Neumann. Contact angle measurements and contact angle interpretation. *Adv. Colloid Interface Sci.*, 81:167–249, 1999.

[17] A. M. Worthington. On the forms assumed by drops of liquids falling vertically on a horizontal plate. *Proc. Roy. Soc. London*, 25:261, 1876.

[18] M. Bussman, J. Mostaghimi, and S. Chandra. On a three-dimensional volume tracking model of droplet impact. *Phys. Fluids*, 11(6):1406–1417, 1999.

[19] J. Fukai, Z. Zhao, D. Poulikakos, M. Megaridis, and O. Miyatake. Modeling the deformationof a liquid droplet impinging upon a flat surface. *Phys. Fluids A*, 5(11):2588, 1993.

[20] J. Fukai, Y. Shiiba, T. Yamamoto, O. Miyatake, D. Poulikakos, C. M. Megaridis, and Z. Zhao. Wetting effects on the spreading of a liquid droplet colliding with a surface : experiment and modeling. *Phys. Fluids*, 7(2):236–247, 1995.

[21] M. B. Lesser. Analytical solutions of liquid-drop impact problems. *Proc. R. Soc. London A*, 377, 1981.

[22] S. E. Bechtel, D. B. Bogy, and F. E. Talke. Impact of a liquid drop against a flat surface. *IBM J. Res. Develop*, 25, 1981.

[23] J. Madejski. Solidification of droplets on a cold surface. *Int. J. Heat Mass Transfer*, 19:1009–1013, 1976.

[24] T. Bennet and D. Poulikakos. Splat-quench solidification: estimating the maximum spreading of a droplet impacting a solid surface. *J. Mater. Sci.*, 29:2025, 1994.

[25] S. L. Manzello and J. C. Yang. On the collision dynamics of a water droplet containing an additive on a heated solid surface. *Proc. R. Soc. Lond. A*, 458:2417, 2002.

[26] N. Mourougou-Candoni, B. Prunet-Ford, F. Legay, and M. Vignes-Adler. Refraction phenomenon of surfactant solution dropls upon impact on a solid substrate of low surface energy. *Langmuir*, 15:6563, 1999.

[27] V. Bergeron, D. Bonn, J. Y. Martin, and L. Vovelle. Controlling droplet deposition with polymer additives. *Nature*, 405, 2000.

[28] W. H. Healy, J. G. Hartley, and S. I. Abdel-Khalik. Surface wetting effects on the spreading of liquid droplets impacting a solid surface at low weber numbers. *Int. J. Heat Mass Transfer*, 44:235–240, 2001.

[29] M. Pasandideh-Fard, Y. M. Qiao, S. Chandra, and J. Mostaghimi. Capillary effects during droplet impact on a solid surface. *Phys. Fluids*, 8:650, 1996.

[30] N. Frayse, M. P. Valignat, A. M. Cazabat, F. Heslot, and P. Levinson. The spreading of layered microdroplets. *J. Colloid Interface Sci.*, 158:27–32, 1993.

[31] L. M. Hocking and A. D. Rivers. The spreading of a drop by capillary action. *J. Fluid Mech.*, 121:425–442, 1982.

[32] R. G. Cox. The dynamics of the spreading of liquids on a solid surface. part 1. viscous flow. *J. Fluid Mech.*, 168:169, 1986.

[33] Z. Zhao, D. Poulikakos, and J. Fukai. Heat transfer and fluid dynamics during collision of a liquid droplet on a solid substrate -i. modeling. *Int. J. Heat Mass Transfer*, 39:2771, 1996.

[34] S. C. Yao and K. J. Choi. Heat transfer experiments of monodispersed vertically impacting sprays. *Int. J. Multiphase Flow*, 13:639, 1987.

[35] I. Mudawar and W. S. Valentine. Determination of the local quench curve for spray cooled metallic surfaces. *J. Heat Treating*, 7:107, 1989.

[36] P. J. Halvorson, R. J. Carson, S. M. Jeter, and S. I. Abdel-Khalik. Critical heat flux limits for a heated surface impacted by a stream of liquid droplets. *ASME J. Heat Transfer*, 116:679, 1994.

[37] S. L. Manzello and J. C. Yang. An experimental study of high Weber number impact of methoxy-nonafluorobutane $C_4F_9OCH_3$(HFE-7100) and n-heptane droplets on a heated solid surface. *Int. J. Heat Mass Transfer*, 45:3961, 2002.

[38] D. M. Anderson, M. G. Forest, and R. Superfine. A model for the spreading and melting droplet on a heated substrate. *Siam J. Appl. math.*, 61:1502–1525, 2001.

[39] Martin Rein. Phenomenon of liquid drop impact. *Fluid Dynamics Research*, 12:61, 1993.

[40] H.-Y. Kim and J.-H. Chun. The recoil of liquid droplets upon collision with solid surfaces. *Phys. Fluids*, 13(3):643–659, 2001.

[41] C. Bohm, D. A. Weiss, and C. Tropea. Multi-droplet impact onto solid walls: droplet-droplet interactions and collision of kinematic discontinuities. *Darmstadt*, pages 11–13, 2000.

[42] W. H. Healy, J. G. Hartley, and S. I. Abdel-Khalik. Comparison between theoretical models and experimental data for the spreading of liquid droplets impacting a solid surface. *Int. J. Heat Mass Transfer*, 39(14):3079–3082, 1996.

[43] H. Jones. Cooling, freezing and substrate impact of droplets formed by rotary atomization. *J. Phys. D: Appl. Phys.*, 4:1657, 1971.

[44] H. Jones. Splat cooling and metastable phases. *Rep. Prog. Phys.*, 36:1425–1497, 1973.

[45] E. W. Collings, A. J. Markworth, J. K. McCoy, and J. H. Saunders. Splat-quench solidification of freely falling liquid-metal drops by impact on a planar substrate. *J. Mater. Sci.*, 25:3677–3681, 1990.

[46] M. H. Shi and J. C. Chen. Behaviour of a liquid droplet impinging on a solid surface. Technical report, ASME 83-WA/HT-104, 1983.

[47] D. Richard. *Situations de mouillage nul.* PhD thesis, University of Paris 6, 2000.

[48] T. Mao, D. C. S. Kuhn, and H. Tran. Spread and rebound of liquid droplets upon impact on flat surfaces. *AIChE J.*, 43:2169–2179, 1997.

[49] D. Y. Kwok, A. Leung, C. N. C. Lam, R. Wu, and A. W. Neumann. Low-rate dynamic contact angles on poly(methyl methacrylate) and the determination of solid surface tensions. *J. Colloid Interface Sci.*, 206:44, 1998.

[50] D. Y. Kwok, A. Leung, A. Li, C. N. C. Lam, R. Wu, and A. W. Neumann. Low-rate dynamic contact angles on poly(n-butly methacrylate) and the determination of solid surface tensions. *Colloid Polym. Sci.*, 276:459, 1998.

[51] D. Y. Kwok, C. N. C. Lam, A. Li, and A. W. Neumann. Low-rate dynamic contact angles on poly(methyl methacrylate/n-butly methacrylate) and the determination of solid surface tensions. *J. Adhesion*, 68:229, 1998.

[52] W. H. Healy. *Modeling the impact of a liquid droplet on a solid surface.* PhD thesis, Georgia Institute of Technology, 1999.

[53] R. Rioboo, M. Marengo, and C. Tropea. Time evolution of liquid drop impact onto solid, dry surfaces. *Experiments in Fluids*, 33:112–124, 2002.

[54] C. D. Bain and G. M. Whitesides. Modeling organic-surfaces with self-assembled monolayers. *Angew. Chem. Int. Ed.*, 28(4):506, 1989.

[55] G. M. Whitesides and P. E. Laibinis. Wet chemical approaches to the characterization of organic-surfaces-self-assemled monolayers, wetting, and physical organic-chemistry of the solid liquid interface. *Langmuir*, 1990.

[56] L. H. Dubois and R. G. Nuzzo. Synthesis, structure, and properties of model organic-surfaces. *Ann. Rev. Mater. Sci.*, 43, 1992.

[57] Y. Xia and G. M. Whitesides. Soft lithography. *Angew. Chem. Int. Ed.*, 37:550, 1998.

[58] Abraham Ulman. Formation and structure of self-assembled monolayers. *Chem. Rev.*, 96:1533–1554, 1996.

[59] I. V. Roisman, R. Rioboo, and C. Tropea. Normal impact of a liquid drop on a dry surface: model for spreading and receding. *Proc. R. Soc. London A*, 458:1411–1430, 2002.

[60] Jun Yang, Jingmin Han, Kelvin Isaacson, and Daniel Y. Kwok. Effects of surface defects, polycrystallinity, and nanostructure of self-assembled monolayers for Octadecanethiol adsorbed onto Au on wetting and its surface energetic interpretation. *Langmuir*, 19:9231–9238, 2003.

[61] C. D. Bain, E. B. Troughton, Y.-T. Tao, J. Evall, G. M. Whitesides, and R. G. Nuzzo. Prospecting for gold: self-assembly on old CDs. *J. Am. Chem. Soc.*, 111:321–335, 1989.

[62] J. Zhang, K. Grundke, and D. Y. Kwok. Comment on "surface characterization of hydrosilylated polypropylene: contact angle measurement and atomic force microscopy". *Langmuir*, 19:10457, 2003.

[63] Y. C. Huang, F. G. Hammitt, and W.-J. Yang. Hydrodynamic phenomena during high-speed collision between liquid droplet and rigid plane. *J. Fluids Eng., Trans. ASME*, 95:276–294, 1973.

[64] F. P. Bowden and J.E. Field. The brittle fracture of solids by liquid impact, by solid impact, and by shock. *Proc. R. Soc. London A*, 282:331–352, 1964.

[65] P. E. Laibinis, B. J. Palmer, Seok-Won Lee, and G. K. Jennings. The Synthesis of Organothiols and their Assembly into Monolayers on Gold. *Thin Films*, 24, 1998.

[66] J. Zhang and D. Y. Kwok. A new method to determine zeta potential and slip coefficient simultaneously. *J. Phys. Chem. B*, 106:12594, 2002.

[67] J. Zhang and D. Y. Kwok. Combining rule for molecular interactions derived from macroscopic contact angles and solid-liquid adhesion patterns. *Langmuir*, 19:4666, 2003.

[68] K.F. Loehr and A. Lasek. Splashing of drops. *Arch. Mech.*, 42(4-5):507–513, 1990.

[69] S. F. Kistler. Hydrodynamics of wetting. In *Wetting (ed. J. C. Berg)*, pages 311–429. New York: Marcel Dekker, 1993.

[70] T. Saburo. A study of mist cooling (2nd report: Theory of mist cooling and its fundamental experiments). *Heat Transfer - Japanese Research*, 1(3):39, 1972.

[71] W. J. Yang. Theory on vaporization and combustion of liquid drops of pure substances and binary mixtures on heated surfaces. 535, Institute of Space and Aeronautical Science, University of Tokyo, Tokyo, 1975.

[72] E. W. Collings, A. J. Markworth, J. K. McCoy, and J. H. Saunders. Splat-quench solidification of freely falling liquid-metal drops by impact on a planar substrate. *J. Mater. Sci*, 25, 1990.

[73] R. E. Ford and C. G. L. Fumidge. Impact and spreading of spray drops on foliar surface. *Wetting, Soc. Chem. Ind.*, Monograph 25:417, 1967.

[74] A. W. Neumann. Contact angles and their temperature dependence: thermodynamic status, measurement, interpretation and application. *Adv. Colloid Interface Sci.*, 4:105, 1974.

[75] R. Bhola and S. Chandra. Freezing of droplets colliding with a cold surface. *ASME HTD*, 306:181, 1995.

[76] H. Fukanuma and A. Ohmori. Behavior of molten droplets impinging on flat surfaces. In *Proceedings of the 7th National Thermal Spray Conference*, pages 563–568, Boston, MA, June 1994.

[77] Y. Rotenberg, L. Boruvka, and A.W. Neumann. Determination of surface tension and contact angle from the shapes of axisymmetric fluid interfaces. *J. Colloids Interface Sci.*, 93:169, 1983.

[78] P. Cheng, D. Li, L. Boruvka, Y. Rotenberg, and A.W. Neumann. Automation of axisymmetric drop shape analysis for measurements of interfacial tensions and contact angles. *Colliods Surfaces A.*, 43:151–167, 1990.

[79] G. K. Jennings and P. E. Laibinis. Self-assembled $n-alkanethiolate$ monolayers on underpotential deposited adlayers of silver and copper on gold. *J. Am. Chem. Soc.*, 119:5208–5214, 1997.

[80] R. F. Allen. The role of surface tension in splashing. *J. Colloid Interface Sci.*, 51:350–351, 1975.

[81] J. S. Hadamard. Slow permanent motion of a viscous liquid sphere in a viscous fluid. *C. R. Acad. Sci.*, 152:1735–1738, 1911.